Defense Threat Reduction Agency
8725 John J. Kingman Road, MS
6201 Fort Belvoir, VA 22060-6201

DTRA-TR-12-64

TECHNICAL REPORT

A Basic Research for the Development and Evaluation of Novel MEMS Digital Accelerometers

Approved for public release, distribution is unlimited.

February 2013

HDTRA1-08-1-0026

Weinong W. Chen et al.

Prepared by:
Purdue University
701 West Stadium Avenue
West Lafayette, IN 47907

REPORT DOCUMENTATION PAGE

Form Approved
OMB No. 0704-0188

1. REPORT DATE *(DD-MM-YYYY)*
00-02-2013

2. REPORT TYPE
Technical

3. DATES COVERED *(From - To)*
4/1/2008 - 3/31/2011

4. TITLE AND SUBTITLE
A Basic Research for the Development and Evaluation of Novel MEMS Digital Accelerometers

5a. CONTRACT NUMBER

5b. GRANT NUMBER
HDTRA1-08-1-0026

5c. PROGRAM ELEMENT NUMBER

6. AUTHOR(S)
Weinong W. Chen, Dimitrios Peroulis, and Alina Alexeenko

5d. PROJECT NUMBER

5e. TASK NUMBER

5f. WORK UNIT NUMBER

7. PERFORMING ORGANIZATION NAME(S) AND ADDRESS(ES)
Purdue University
701 West Stadium Avenue
West Lafayette, IN 49707-2045

8. PERFORMING ORGANIZATION REPORT NUMBER

9. SPONSORING / MONITORING AGENCY NAME(S) AND ADDRESS(ES)
Defense Threat Reduction Agency
8725 John J. Kingman Road STOP 6201
Fort Belvoir, VA 22060
PM/ D. Petersen

10. SPONSOR/MONITOR'S ACRONYM(S)
DTRA

11. SPONSOR/MONITOR'S REPORT NUMBER(S)
DTRA-TR-12-64

12. DISTRIBUTION / AVAILABILITY STATEMENT
Approved for public release; distribution is unlimited.

13. SUPPLEMENTARY NOTES

14. ABSTRACT

This research program develops fundamental understandings necessary for producing novel MEMS/NEMS acceleromters that characterize impact motion with high-precision, high-redundancy, high-frequency-response, high reliability, and high manufacturing repeatability. The accelerometers developed in this research consume a small fraction of power as compared to conventional accelerometers, which makes them ideal choices for applications where available power is limited. This is achived through the design, fabrication,packaging, and testing of a novel high-g MEMS accelerometer. Cantilever beams corresponding to different acceleration levels of 20,000-40,000g are fabricated on low resistivity on (<0.01 Ω-cm) silicon on insulator wafers (SOI). The beams are fabricated in a 0.3 cm by 0.3 cm die which is then packaged and wire bonded in a ceramic package, which is then mechanically shocked for testing and evaluation. Due to the feasibility demonstrated in this research program, the novel accelerometers developed have strong potentials to be adapted in applications in the future.

15. SUBJECT TERMS
MEMS, accelerometer, NEMS, cantilevers

16. SECURITY CLASSIFICATION OF:

a. REPORT	**b. ABSTRACT**	**c. THIS PAGE**	**17. LIMITATION OF ABSTRACT**	**18. NUMBER OF PAGES**
Unclassified	Unclassified	Unclassified	SAR	50

19a. NAME OF RESPONSIBLE PERSON
David Petersen

19b. TELEPHONE NUMBER *(include area code)*
703-767-3164

Standard Form 298 (Rev. 8-98)
Prescribed by ANSI Std. Z39.18

CONVERSION TABLE

Conversion Factors for U.S. Customary to metric (SI) units of measurement.

MULTIPLY → BY → TO GET

TO GET ← BY ← DIVIDE

angstrom	1.000 000 x E -10	meters (m)
atmosphere (normal)	1.013 25 x E +2	kilo pascal (kPa)
bar	1.000 000 x E +2	kilo pascal (kPa)
barn	1.000 000 x E -28	meter^2 (m^2)
British thermal unit (thermochemical)	1.054 350 x E +3	joule (J)
calorie (thermochemical)	4.184 000	joule (J)
cal (thermochemical/cm^2)	4.184 000 x E -2	mega joule/m^2 (MJ/m^2)
curie	3.700 000 x E +1	*giga bacquerel (GBq)
degree (angle)	1.745 329 x E -2	radian (rad)
degree Fahrenheit	$t_k = (t^{\circ}f + 459.67)/1.8$	degree kelvin (K)
electron volt	1.602 19 x E -19	joule (J)
erg	1.000 000 x E -7	joule (J)
erg/second	1.000 000 x E -7	watt (W)
foot	3.048 000 x E -1	meter (m)
foot-pound-force	1.355 818	joule (J)
gallon (U.S. liquid)	3.785 412 x E -3	meter^3 (m^3)
inch	2.540 000 x E -2	meter (m)
jerk	1.000 000 x E +9	joule (J)
joule/kilogram (J/kg) radiation dose absorbed	1.000 000	Gray (Gy)
kilotons	4.183	terajoules
kip (1000 lbf)	4.448 222 x E +3	newton (N)
kip/inch^2 (ksi)	6.894 757 x E +3	kilo pascal (kPa)
ktap	1.000 000 x E +2	newton-second/m^2 (N-s/m^2)
micron	1.000 000 x E -6	meter (m)
mil	2.540 000 x E -5	meter (m)
mile (international)	1.609 344 x E +3	meter (m)
ounce	2.834 952 x E -2	kilogram (kg)
pound-force (lbs avoirdupois)	4.448 222	newton (N)
pound-force inch	1.129 848 x E -1	newton-meter (N-m)
pound-force/inch	1.751 268 x E +2	newton/meter (N/m)
pound-force/foot^2	4.788 026 x E -2	kilo pascal (kPa)
pound-force/inch^2 (psi)	6.894 757	kilo pascal (kPa)
pound-mass (lbm avoirdupois)	4.535 924 x E -1	kilogram (kg)
pound-mass-foot^2 (moment of inertia)	4.214 011 x E -2	kilogram-meter^2 (kg-m^2)
pound-mass/foot^3	1.601 846 x E +1	kilogram-meter^3 (kg/m^3)
rad (radiation dose absorbed)	1.000 000 x E -2	**Gray (Gy)
roentgen	2.579 760 x E -4	coulomb/kilogram (C/kg)
shake	1.000 000 x E -8	second (s)
slug	1.459 390 x E +1	kilogram (kg)
torr (mm Hg, 0^0 C)	1.333 22 x E -1	kilo pascal (kPa)

*The bacquerel (Bq) is the SI unit of radioactivity; 1 Bq = 1 event/s.

**The Gray (GY) is the SI unit of absorbed radiation.

Executive Summary

A Basic Research for the Development and Evaluation of Novel MEMS Digital Accelerometers

DTRA Grant: HDTRA1-08-1-0026

Period of Performance: 01 April 2008 through 31 March 2011

PI: Weinong Wayne Chen, Purdue University

Co-PIs: Dimitrios Peroulis and Alina Alexeenko, Purdue University

The goal of this research program is to develop fundamental understandings necessary for producing novel MEMS/NEMS accelerometers that will characterize impact motion with high-precision, high-redundancy, high-frequency-response, high reliability, and high manufacturing repeatability. Such accelerometers consume a small fraction of power as compared to conventional accelerometers, which makes them ideal choices for applications where available power is limited.

A novel high–g MEMS digital accelerometer has been designed, fabricated, packaged, and tested. Cantilever beams corresponding to the different acceleration levels are fabricated on low resistivity (<0.01 Ω-cm) silicon on insulator wafers (SOI) using standard micromachining techniques. Cantilevers created from SOI wafers have uniform single-crystal nature, negligible and repeatable residual stress. The cantilevers have spring constants in the order of 184 – 462 N/m for a deflection of 2 μm corresponding to different acceleration levels of 20,000–40,000 g. This in turn corresponds to beams of length 533-630 μm and width 70-100 μm and thickness of 20 μm. The beams are fabricated in a 0.3 cm by 0.3 cm die which is then packaged and wire bonded in a ceramic package, which is then placed in a tungsten carbide package and potted with STYCAST 1090SI for shock testing and evaluation. Laboratory controlled shock experiments evaluate and calibrate the novel accelerometers. The results from these experiments show that the devices turn on when the acceleration crossed the designed acceleration threshold and turns off once the acceleration falls below the threshold. The switching mechanism is modeled considering the damping effects from the gas in the 2 μm gap. The switching time, in the order of 0.1μs, was found to be in close correspondence with the analytical calculations for a similar acceleration profile. Analysis is being conducted on the failure of the silicon beams as the size decreases and loading rate increases.

Due to the feasibility demonstrated in this research program, the novel accelerometers developed have strong potentials to be adapted in applications in the near future. This report summarizes the technical achievements realized during the performance period of this research program.

Table of Contents

1. Introduction

1.1 *Background*

With recent advances in high-g applications, there is an increased need to monitor acceleration fluctuations in the several 10,000s g range. Such acceleration levels are typical in impact and pyroshock phenomena and are commonly observed in multistage rocket launches and earth penetrating weapon detonations. Currently, high-g accelerometers have been of the conventional spring-mass type with piezoelectric and capacitive sensing and have their limitations under such loads.

The most commercially used piezoelectric accelerometer of this type is the Endevco 7270 series which can be used to measure acceleration histories up to 200,000 g. However, a history of failure under lower-g shock loads has been seen in such accelerometers. For instance, 200,000-g accelerometers have failed under 10,000-g shock loads. Analysis on the failure modes of this accelerometer can be found in [1]. In about half of the devices that failed, failure was due to the damage to the proof mass. Given that no redundancy exists, failure in the proof mass leads to a total failure in the accelerometer.

Another commercial accelerometer is the Silicon Design 1220, which is similar in design to the SDI 1210. Sensing in this accelerometer is of the capacitive type with a max detection of 6,000 g. These were found to suffer from a time shift in the output and fail under shock loads of about 70,000 g due to damage to the sensing electrodes and proof mass [2].

The Analog Devices ADX 181-100 is another state-of-the-art capacitive accelerometer, which measures acceleration level up to 1,000 g via capacitive sensing. The unique feature of this accelerometer is that sensing is done via 40 individual sensing cells with each cell measuring acceleration independently, thus offering redundancy to the device. However the acceleration pulse width detected by this accelerometer was found to be less than the actual applied profile. In addition, there was a lag in detection (up to 260 μs) when subjected to shock loads [2].

Researchers from Sandia National Labs have also developed a capacitive high-g accelerometer. This has been shown to detect accelerations level up to 46,000 g. There is a significant latency in the detection from this accelerometer when compared to the applied acceleration profile [1].

Consequently, it can be seen that existing devices offer limited redundancy, high noise output and latency in detection [3], [4] for typical high-g loads. In order to overcome these limitations, we propose a system consisting of an array of single-crystal silicon (SCS) micro-beams that respond to different acceleration levels by having multiple beams making solid-to-solid contacts for a given acceleration level This method has been shown to offer high redundancy and ensures an adequate confidence level in the measure data. This is critical when this sensor is used to trigger events with potential severe consequences. Furthermore, laboratory controlled shock experiments have been developed to evaluate and calibrate the novel SCS accelerometers. In addition, analytical and numerical models are developed to predict the damping characteristics of the SCS micro-beams. The results from the validation shock experiments indicate that the performance of the novel accelerometers agree well with design goals and model predictions.

2. Technical Approach

2.1 *Development of MEMS Accelerometer*

2.1.1 System Overview

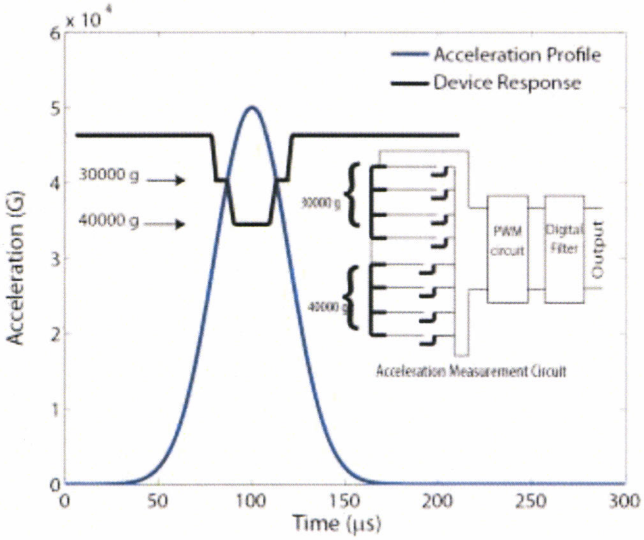

Figure 1: Overview of the proposed accelerometer design.

The design concept for the proposed accelerometer that can be created using cantilevers is shown in Figure 1. In this design concept, a number of single-crystal silicon MEMS cantilevers are connected in parallel with the measuring circuit shown. This leads to a "piano approach" in acceleration detection with each set of beams responding to a designed acceleration level. The needed number of beams for each acceleration level depends on the desired confidence level needed for the measurement. When the system is subjected to the acceleration profile shown in Figure 1, a Pulse Width Modulated (PWM) circuit (described in Section 2.3) reads the raw response. The response from this circuit is then processed with a microprocessor acting as a digital filter in order to filter the noise spikes and contact bouncing due to impact vibrations.

Previous research has provided some insight on the impact phenomena on typical MEMS DC switches, particularly on their failure such under such impact load conditions [5], [6]. However, little work on the dynamic behavior of silicon-to-silicon contact cantilevers has been completed.

In order to effectively design the accelerometer for high-g loads, we need to gain a fundamental understanding of the behavior of silicon MEMS cantilevers under high-g loading. This includes the following main characteristics

1) Silicon as a fabrication material & silicon to silicon contacts
2) High-g loading on MEMS structures
3) Failure mechanism of micro-contacts.

2.1.2 Silicon as a Fabrication Material

In order to design and fabricate an effective MEMS accelerometer we needed to choose a suitable fabrication material. Single-crystal silicon is ideal for micromechanical moving structures due to its a) nearly defect-free nature, b) immunity to process-induced material-property variations (properties of silicon wafers are extremely well controlled), c) creep-free structure, and d) the wide manufacturing basis of silicon electronics. For instance, research reported at [7] has shown silicon to be creep free as indicated in Figure 2.

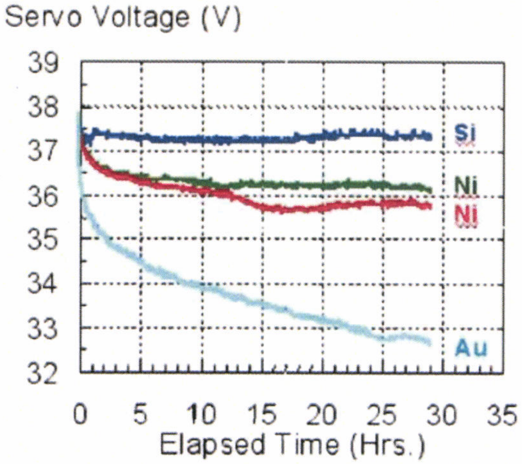

Figure 2: Long term needed bias to maintain a constant deflection for different cantilever materials in air [7].

Since the proposed MEMS device works by sensing a close-or-open contact, a suitable contact material need to be decided for ideal operation under high-g loads. The contact material for such conditions should exhibit low adhesion forces, high resistance to impact damage, and potential for repeatable low-cost fabrication particularly in a CMOS foundry. Silicon satisfies well these requirements and was chosen as a contact material as well. In addition, the formation of native oxide on this material during operation gives it the potential for self–healing.

Silicon-to-silicon contacts have not been adequately characterized in the literature. To the best of our knowledge, this is the first application that utilizes silicon for electronic contacts. As a result, we investigated its suitability for this application in years 1 and 2. Test structures were fabricated on Silicon-on-Insulator (SOI) wafer with a device and handle layer resistivity of 0.01 Ω-cm and device layer thickness of 2 μm using the fabrication process shown in Figure 3. These test structures included cantilever and fixed-fixed beams of varying lengths and widths and were electrostatically actuated to simulate contact forces during high-g loads.

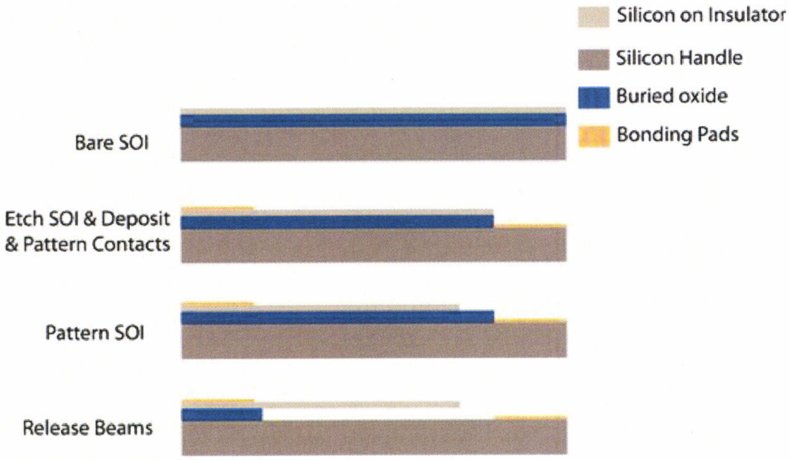

Figure 3: Fabrication process for silicon test structures

The devices fabricated using the fabrication process are shown in Figure 4.

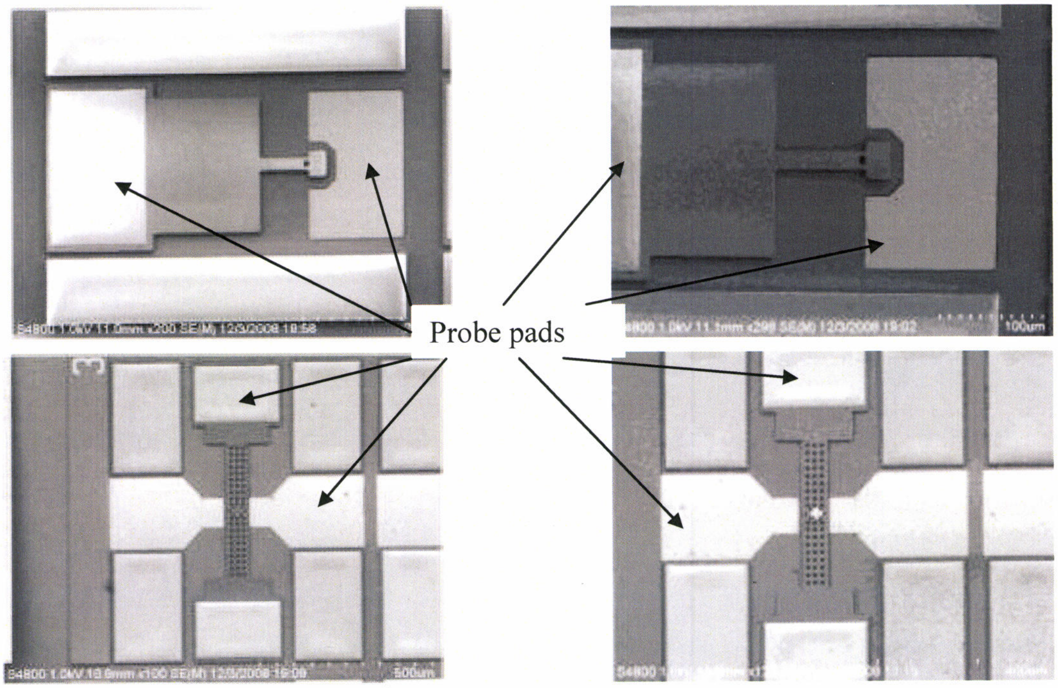

Figure 4: Fabricated silicon test structures.

These devices were electrostatically actuated and were found to have actuation voltages between 20-30 V and contact resistances in the order of 3-4 kΩ (Figure 5). These results show that silicon to silicon contacts are well-suited for measuring contact based events such as the one proposed in this project. Although repeatability was not formally characterized, no degradation was observed in our laboratory after many 100s of cycles even in an open unpackaged environment.

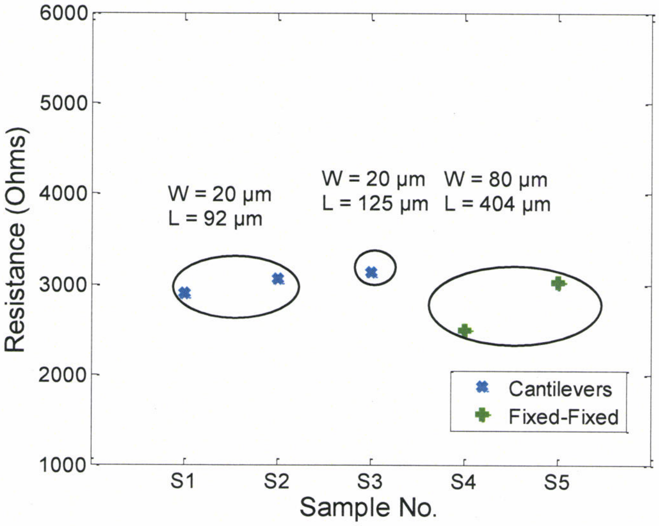

Figure 5: Contact resistance of the silicon test structures

2.1.3 *High-g MEMS Design Fundamentals*

With the contact and the fabrication material chosen, the first functional high-g switches were designed in year 2. This design consisted of cantilevers of different spring constants corresponding to different acceleration levels of up to 46,000 g. A typical fabrication result of the "piano approach" is shown in Figure 6. The cantilever beams were initially designed using the dynamic equations of motion shown below [8] (more accurate modeling is included in Section 2.2)

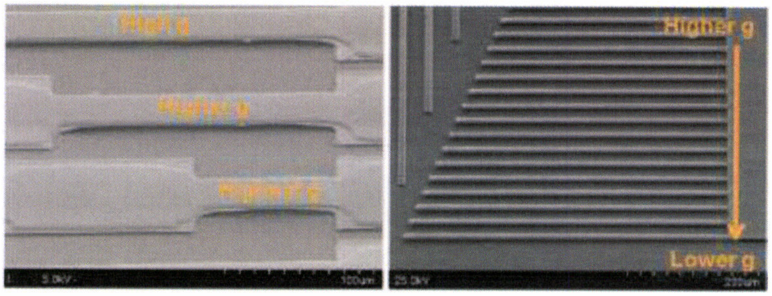

Figure 6: Typical fabrication results of the "piano approach" for the MEMS digital accelerometers.

$$m\frac{d^2x}{dt^2} + b\frac{dx}{dt} + k \times x = F_{acc} + F_c \tag{1}$$

where

F_{acc} = Force due to acceleration
x = deflection gap
m = mass of the beam
b = damping factor ($b = k/\omega^0 Q$)
Q = Quality factor
F_c = Contact forces (Van der Waals Forces and the repulsive contact forces)

Where k is the spring constant of the cantilever under a distributed load and is given by the following equation.

$$k = \frac{2}{3}\frac{Ewh^3}{L^3} \tag{2}$$

where
w = width of the beam
h = thickness of the beam
L = length of the beam

Assuming a width of 100 μm, thickness of 20 μm, deflection of 2 μm and a contact force of 50 μN, the spring constant and the length versus acceleration are plotted below.

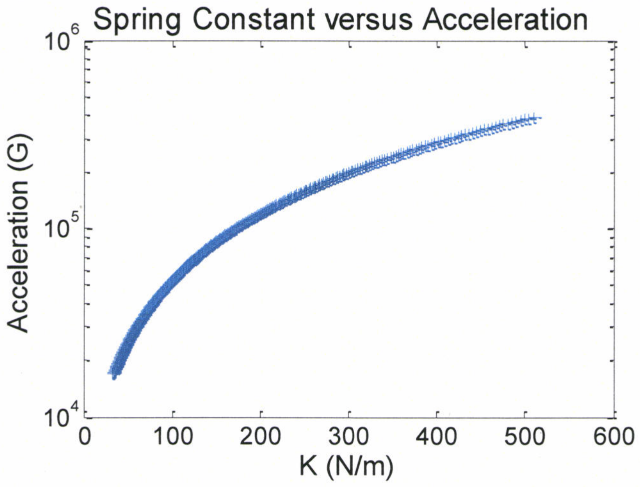

Figure 7a: Spring Constant versus acceleration

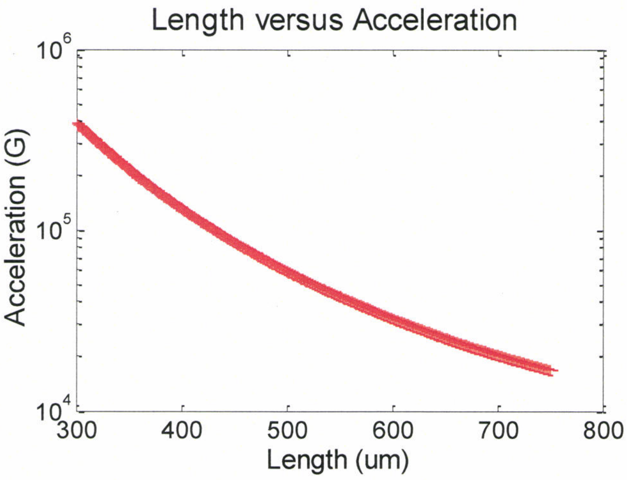

Figure 7b: Length versus acceleration

From the above graphs we can see that the spring constants of the beams are in the ranges of 80-400 N/m in order to measure accelerations of 5,000-40,000 g. The design process was repeated to explore beams design for a width of 70 μm.

Using the above graphs and design equations, beams corresponding to three different accelerations levels were chosen. A summary of different parameters that were chosen are shown in *Table 1* below.

Table 1 : Summary of the design parameters

Acceleration Level (g)	**Length (µm)**	**Width (µm)**	**Thickness (µm)**
20000	630	100	20
30000	572	100	20
40000	530	100	20
20000	640	70	20
30000	576	70	20
40000	533	70	20

2.1.4 Fabrication Process Flow

Using the above designed values, a fabrication process for the actual MEMS accelerometers was developed. In year 1, cantilever beams corresponding to the different acceleration levels were fabricated on SOI wafers with handle and device resistivity of <0.01 Ω-cm using standard micromachining techniques as shown in Figure 3. The bare SOI wafer is patterned and etched to reach the handle layer. A metal layer of Cr/Au was then deposited and patterned to create the contacts. In the next step, the SOI layer is patterned and etched using Deep Reactive Ion Etching (DRIE) to create the cantilevers. The final step in the fabrication process is the release of the cantilevers using controlled etching of the oxide using a mixture of HF and water in the ratio of 1:4. The released structures are carefully transferred to water and then transferred to solutions of Acetone, Methanol and then Isopropyl Alcohol for duration of 5 minutes each. The samples are then dried using a Critical Point Drying (CPD) process. The entire fabrication process takes a total of three masks.

In year 3, the fabrication process was optimized to create a more robust one shown in Figure 8. The bare SOI wafer is first patterned and etched using DRIE to create the cantilevers. Then Photoresist (PR) is deposited and patterned to create a lift off mask. The same mask is used to etch the oxide to reach the handle layer. A metal layer of Cr/Au is then deposited and lifted off to create the contacts on the handle and device layers. The next step involves the patterning of the cantilevers using DRIE. The final step in the fabrication process is the release which is then preformed as mentioned above.

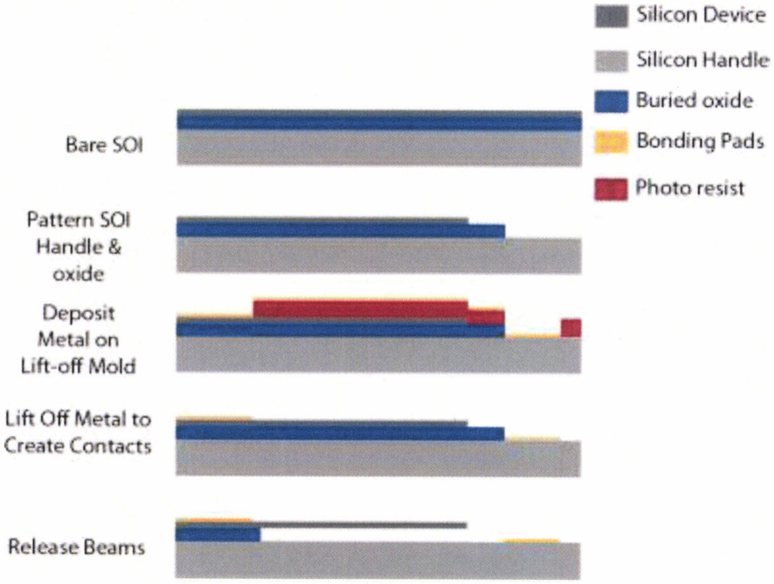

Figure 8: Optimize fabrication process

This fabrication process utilizes only 2 masks. It resulted in substantial higher fabrication yield (nearly all devices on a wafer were successful) and measurement repeatability.

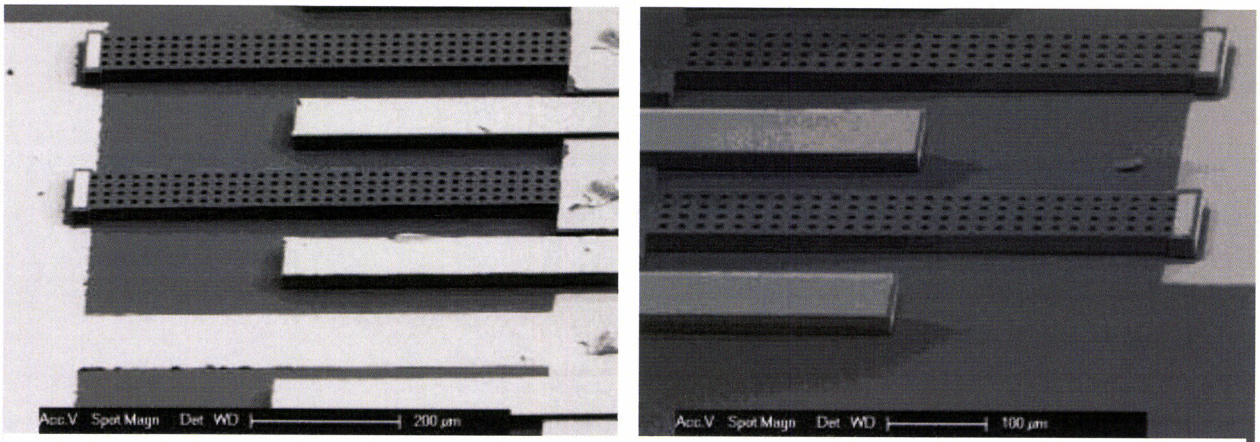

Figure 9: Fabricated g-switches using the optimized fabrication process.

Beams were fabricated for three different acceleration levels from 20,000 g up to 40,000 g for different widths of 70 µm and 100 µm. Figure 9 shows devices fabricated using this process. These then tested under high-g loads as explained in the experimental evaluation section.

2.2 *Modeling and Simulation of Accelerometer Operation*

2.2.1 Problem Definition

The main goals of the modeling and simulation effort for the high-g accelerometer were the following.

- To develop predictive modeling for dynamics of accelerometer beam under all relevant forces, including the fluidic damping and external acceleration.
- To evaluate the modeling by comparison with direct experimental measurements of accelerometer operation under various load levels.
- To determine physical phenomena and parameter ranges critical for design of reliable accelerometer structures.

For microscale devices such as the MEMS accelerometer, inaccuracies arise from straightforward downscaling of conventional macroscale models. For example, because of the small physical scale of the device, the fluid-structure coupling is expected to play an increasingly important role in the dynamic response of the MEMS accelerometer beams. This is because the damping force is a surface phenomenon, whereas inertia is a volume force. As the size of the device is scaled down, the surface-to-volume ratio of a structure increases and thus fluidic damping acquires a larger role in the dynamic response than in large-scale structures. Moreover, the fluidic damping is expected to deviate from the conventional macroscale gas damping because of the extremely small air gap encountered during the approach to contact. Since contact behavior determines the accelerometer performance, this near-contact damping needs to be modeled with high fidelity.

In this regard, the dynamics problem was formulated as follows: **for a set of given geometric and mechanical properties, to determine the unsteady response of accelerometer beam under a specified high-g dynamic load.** The dynamic response of beam is governed by coupling between the inertia, bending and gas damping under the external acceleration from 0 to 10,000s of g. Additionally, short-range forces manifested by repeated contacts, i.e. bouncing, can potentially play a significant role in the accelerometer response after initial closing.

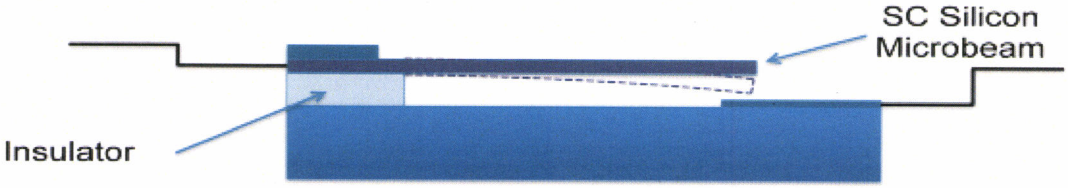

Figure 10: Schematic of accelerometer beam motion in x-y plane.

A schematic of beam response due to external acceleration is shown schematically in Figure 10. Here we will use the following notations: the direction along the length of beam will correspond to x-axis, while the direction normal to the beam is y-axis. A cross-sectional view of the beam with typical dimensions is shown in Figure 11. Note that the air gap, even at its maximum of about 2 μm, is much smaller than the typical minimum dimension of the beam of about 20 μm.

Moreover, the gap is comparable to the mean free path of air molecules, especially when the beam approaches contact.

At standard atmospheric conditions the mean free path of air is about 60 nm. At contact the air gap is effectively equal to just a few nanometers, that is the characteristic size of the surface roughness.

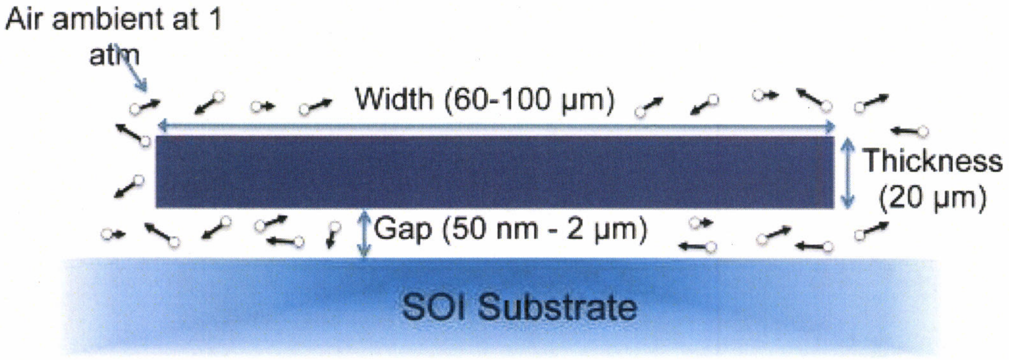

Figure 11: Schematic of accelerometer beam in y-z plane (not to scale).

Because of the small physical scale for the gas damping problem, the standard continuum models of the fluidic damping of such microbeams are expected to break down. This is illustrated by the map of aerodynamic damping regimes for microbeams as shown in Figure 12. The applicability of different fluidic models can be characterized by the Knudsen number, Kn, the ratio of the molecular mean free path, λ, to the characteristic physical scale of the flow. In the case of accelerometer beam motion, the characteristic scale for the gas damping problem is the size of the air gap, g, between the moving beam and the SOI substrate.

For very small values of the Knudsen number, Kn<0.01, i.e. when the gap is much larger than the mean free path, the flow is in the continuum regime. The continuum fluid damping models are usually based on the Reynolds equation, which is a form of Navier-Stokes equations for a case of small bulk flow velocities.

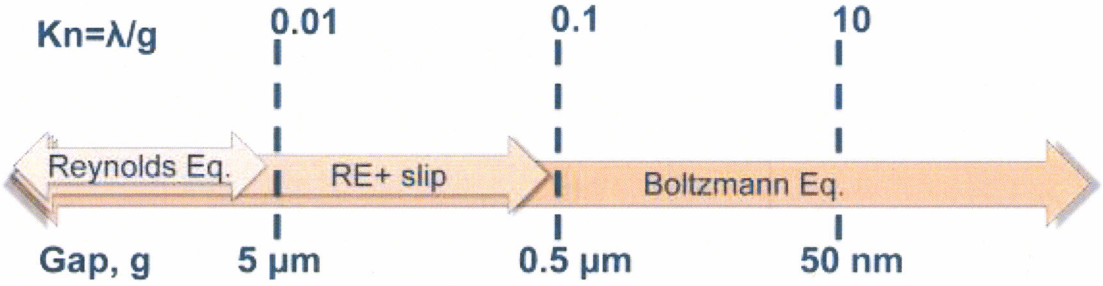

Figure 12: Rarefaction regimes and governing equations for aerodynamic damping in high-h MEMS Accelerometer in air at 1 atmosphere and room temperature.

It can be seen that for a typical beam in the MEMS accelerometer, the initial gap of about 2 μm corresponds to a Knudsen number of about 0.02 which is outside of the continuum flow regime. Typically for $0.01<Kn<0.1$ the continuum model augmented by a velocity slip boundary conditions can give accurate results. However, as the gap between the beam and substrate is further reduced below about 0.5 μm, the slip approximation becomes invalid. The modeling for very small gaps has to be based on the non-continuum Boltzmann kinetic equation for gas molecules.

Note that for MEMS accelerometer the squeeze-film aerodynamic damping occurs in several regimes due to gap size varying from microns to tens of nanometers. Since the Boltzmann equation is valid for arbitrary Knudsen numbers it has been the principal governing equation for gas damping applied in the analysis presented below. The results based on the Boltzmann equation have also been compared with predictions using earlier models based on Reynolds equation with the first-order velocity slip.

2.2.2 Analytical Modeling

The beam dynamics modeling is based on Euler-Beroulli beam theory applied to calculate the beam deflection:

$$\rho A \frac{\partial^2 w(x,t)}{\partial t^2} + EI \frac{\partial^4 w(x,t)}{\partial x^4} + C_f \frac{\partial w(x,t)}{\partial t} = f_{ext}(t) \qquad (3)$$

where ρ is the material density (kg/m^3), A is the beam cross-sectional area (m^2), w is the beam deflection in Z-direction (m), E is the Young's modulus of the material (Pa), I is the moment of inertia (m^4), C_f is the gas damping coefficient (N·s/m) and f_{ext} is the external acceleration pulse (m/s^2).

Thus it was assumed that the majority of the load is applied perpendicular to the beam's length, and consequently there is no axial deflection. The beam was assumed to be fixed on one end and allow free movement on the other end as shown in Figure 10. The beam is assumed initially at rest, $\frac{\partial w(x,0)}{\partial t} = 0$.

Using contact with the surface as another boundary condition and an experimentally observed acceleration profile, the beam deflection as a function of time was generated. Contact was chosen to be when the beam tip deflected to within 50 nm of the surface, giving a theoretical system response for a given acceleration profile.

The dynamic model given by Eq. (3) requires definition of the gas damping coefficient, C_f, which is equal to the gas damping force per unit length, F_{damp}', divided by local beam cross-section velocity, $\frac{\partial w(x,t)}{\partial t}$ i. e

$$C_f(x,t) = \frac{F_{damp}(x)'}{\frac{\partial w(x,t)}{\partial t}}. \qquad (4)$$

The gas damping is in principle dependent on the instantaneous air gap size and can be either in continuum or rarefied regime. As the beam velocity is much smaller than the speed of sound as will be shown later, the non-linear velocity effects in damping have been neglected.

In order to find the damping force on the beam, the following two-dimensional form of the Boltzmann equation is solved:

$$u\frac{\partial f(x,y,u,v)}{\partial x}+v\frac{\partial f(x,y,u,v)}{\partial y}=\frac{f_0(x,y,u,v,n,T,u_0,v_0)-f(x,y,u,v)}{\tau} \qquad (5)$$

where *(u,v)* are gas molecule velocities in the *(x,y)* directions, $\nu = 1/\tau$ is the gas molecule collision relaxation frequency, f is the molecular velocity distribution function, and f_0 - equilibrium distribution function given by the ellipsoidal-statistical Bhatnagar-Gross-Krook (ESBGK) model as

$$f_0(x,y,u,v)=\frac{n(x,y)}{\sqrt{(2\pi)^3\det(\Lambda_{ij})}}\exp(-\frac{\varepsilon_{ij}}{2}\vec{u}'\otimes\vec{u}')$$

where n is the local gas number density, (u_0,v_0) are local bulk gas velocity components. The tensor Λ_{ij} is defined as

$$\Lambda_{ij}=RT\delta_{ij}+(1-\frac{1}{\Pr})\frac{p_{ij}}{\rho}$$

where R is the specific gas constant (J/kg/K), T is the local gas temperature, Pr is the Prandtl number which was assumed to be equal to 0.75 for air, p_{ij} is the non-isotropic local pressure tensor and ρ_{ij} is the local gas mass density.

Once the solution of the Boltzmann-ESBGK equation, Eq. (5) is obtained, the gas damping force can be found as follows. First, the velocity distribution function is integrated over the velocity space to find the spatial distribution of the normal pressure on the top and bottom of the beams well as shear stress on the sides of the beam. Then the obtained stress distribution is integrated across the width of the beam on the top and bottom surfaces and across the thickness on the side surfaces to obtain the damping force per unit length (N/m):

$$F_{damp}'=\int_{-b/2}^{b/2}(p_{zz}(y,z_b)-p_{zz}(y,z_t))dy+2\int_{z_b}^{z_t}p_{yz}(b/2,z)dz \qquad (6)$$

The procedures implemented for obtaining the numerical solutions of Eq. (3) for beam dynamics and Eqns. (5)-(6) for gas damping are described in the following section.

2.2.3 *Numerical Simulation*

The partial differential Eq. (3) for accelerometer beam dynamics was discretized using the finite difference method in time and space. A backward difference in time and central difference in space are employed. The discretized partial differential equations are:

$$\frac{\partial^2 w}{\partial t^2} = \frac{w_i^n - 2w_i^{n-1} + w_i^{n-2}}{\Delta t^2}$$

$$\frac{\partial^4 w}{\partial x^4} = \frac{w_{i-2}^n - 4w_{i-1}^n + 6w_i^n - 4w_{i+1}^n + w_{i+2}^n}{\Delta x^4}$$

The final system of equations for each time step is solved using LAPACK's "dgbsv" subroutine. The numerical method described above has been implemented in FORTRAN 90.

The beam dynamics solver has been verified by comparison with analytical solution obtained for the harmonic excitation of a cantilever beam. Figure 13 shows a comparison of the analytical solution for a cantilever tip displacement as a function of time with the numerical solution. The agreement between the analytical solution and the numerical simulations is within the first seven significant digits, which verifies the correct implementation of the numerical solver for beam dynamics, Eq. (3).

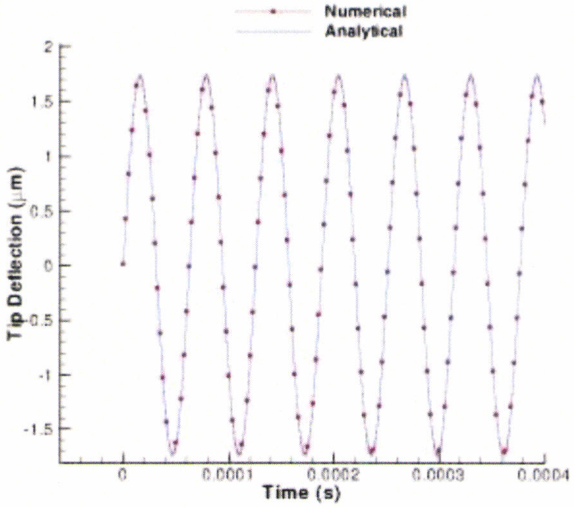

Figure 13: Verification of numerical solution for harmonic excitation of a cantilever beam.

The Boltzmann-ESBGK Eq. (5) was solved using the 2D quasi-steady finite-volume discrete-ordinate solver developed by Alexeenko and co-authors [13, 14]. The solver employs the finite volume method in the physical coordinate space and the discrete-ordinate method in the velocity space. A second-order quadrant splitting scheme is applied in the physical space and a 16-th order Gauss-Hermite quadrature is applied for the velocity magnitude. Verification of the numerical approach and solver has been published earlier.

The numerical simulations were performed for typical accelerometer beam geometries at variable beam to substrate air gap heights. Due to the symmetry of the beam, only the right half of the beam cross-section was included in gas damping simulations. A symmetric boundary condition was applied on the left boundary of the domain. A diffuse-reflection wall boundary condition was used for beam and the substrate surfaces. A relative bulk velocity was applied for the top, bottom and side surfaces of the beam to represent the accelerometer beam motion under the external acceleration. The pressure inlet conditions were applied for the far-field top and right boundaries of the domain. The computational domain extent was chosen to be three times larger than the size of the beam in both dimensions to mitigate the effect of the finite flow velocity at the pressure inlet boundaries. A non-uniform spatial mesh of the size 140×140 grid nodes were used based on grid convergence studies and is shown in Figure 14.

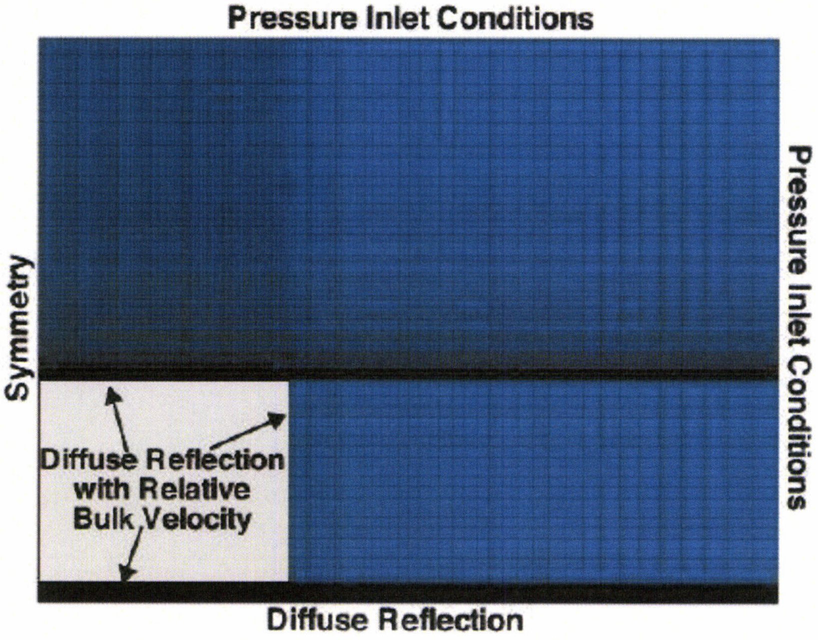

Figure 14: Schematic of boundary conditions and a sample mesh for 2D ESBGK gas damping simulations.

Gas damping simulations were performed at various beam-to-substrate gap heights to capture the variation of the damping force during the accelerometer beam actuation. Although there are published models of gas damping at the microscale, they deal predominantly with small-amplitude motion away from contact. Therefore, a new damping model was developed based on

2D gas damping simulations using the Boltzmann-ESBGK solver specifically for geometries and dynamic conditions encountered in the MEMS accelerometer.

Typical ESBGK simulation results for the gas flow around the moving accelerometer beam are shown in Figures 15 and 16. Figure 15 shows the pressure flow fields around the beam for two air gap values, 0.1 and 1 micron. The corresponding air velocity magnitudes are shown in Figure 16. Note that the beam in both cases is moving downward with a velocity of 0.1 m/s. The flowfields are typical for a squeeze film damping when the gas is being pushed out from a narrow gap between parallel surfaces in relative out-of-plane motion.

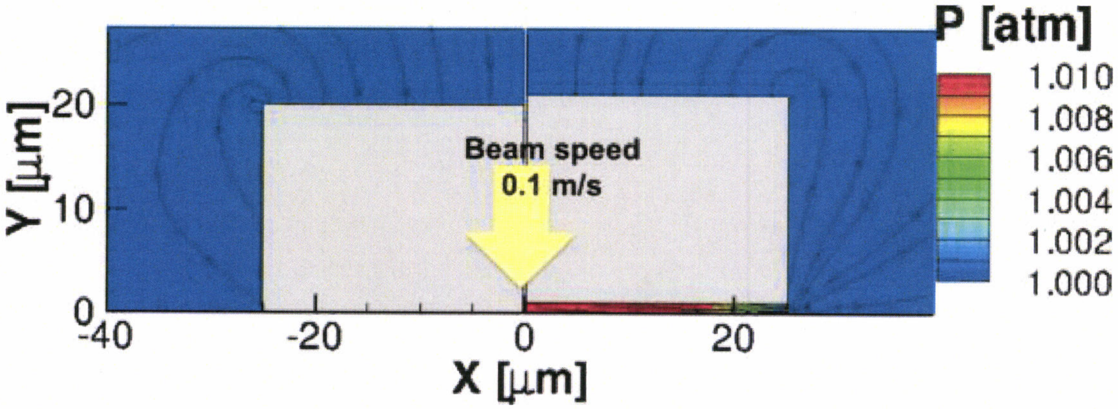

Figure 15: Pressure fields and streamlines for 0.1 µm gap (left) and 1 µm gap (right).

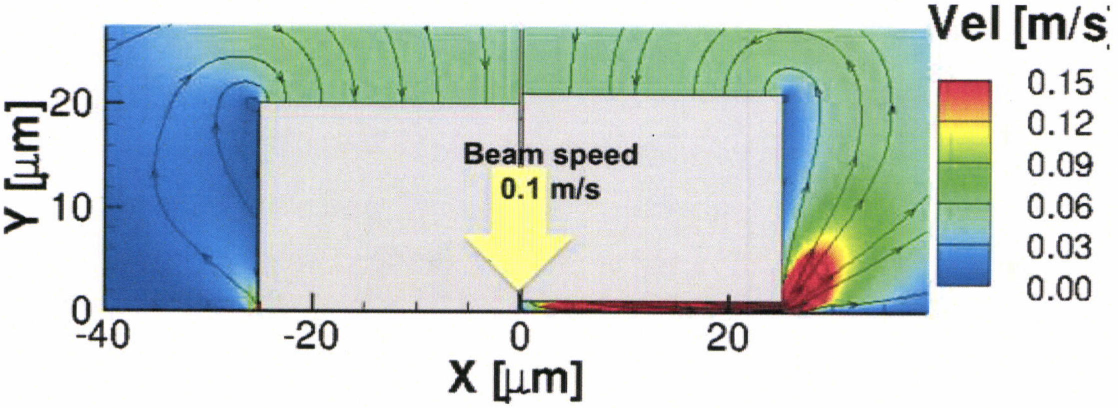

Figure 16: Air speed fields and streamlines for 0.1 µm gap (left) and 1 µm gap (right).

Because of the limited speed with which the air molecules can escape from the gap the air pressure builds up on the bottom of the beam. This is clearly seen in Figure 15. The air velocity field has a vortical structure around the edge of the beam. This is generated by a jet of air that emanates from the beam-to-substrate gap. Note that the jet velocity is higher than that of the beam for the small gaps of the accelerometer beams. The contours in Figure 16 show a gas jet emanating from the gap with speeds that are ~50% higher than the beam velocity itself.

The pressure difference between the bottom and top of the beam leads to the air damping force that opposes the beam motion. The origin and magnitude of such force is illustrated by the distribution of the normal pressure component on the bottom of the beam which is shown in Figure 17. It can be seen that the pressure at the bottom of the beam is about 10% above the atmospheric for 0.1 μm, whereas it is about 2% above for 1 μm gap. The increase in the maximum pressure of about 5 times higher for the 0.1 μm gap as compared to that at 1 μm points to a slower than linear dependence of the damping coefficient on the gap size as it approaches zero. Though the beam velocity itself remains the same for the two cases, the smaller gap leads to a much higher pressure at the bottom surface of the beam leading to a much higher damping.

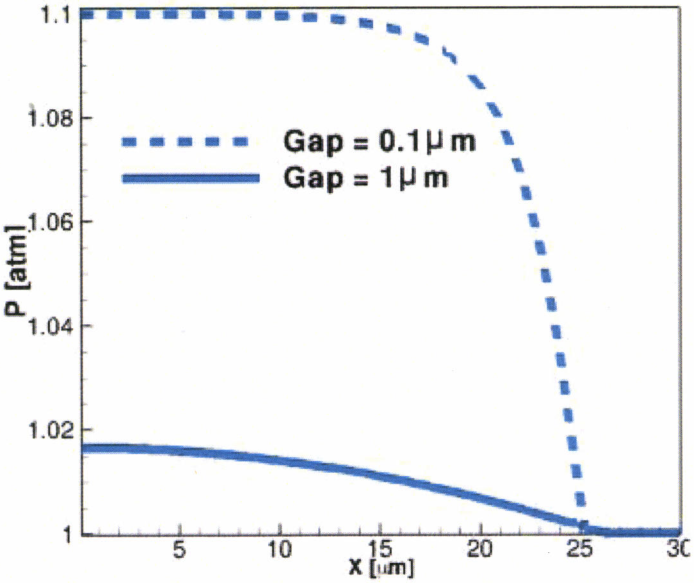

Figure 17: Normal component of pressure profile along bottom of the accelerometer microbeam at 0.1 and 1 μm gap.

The ESBGK simulations were performed for various gap sizes ranging from about 50 nm to 2 μm. The upper limit of 2 μm is selected because it is the typical gap for initially stationary accelerometer beams. The 50 nm lower limit is the estimated effective gap when the beam bottom surface contacts the substrate due to a finite number asperities on both surfaces. Note that the gap between two atomically rough surfaces never goes to zero due to a finite surface roughness.

The computed variation of the gas damping coefficient as a function of gap size obtained using the ES-BGK simulations is shown in Figure 18. Also shown are earlier models from literature. In particular, the thin-beam model [15] is also based on ESBGK simulations but for beam geometries that have width-to-beam ratio of 10 and higher. The model of Gallis and Torcynzski model [16] is obtained also for relatively thin beams and using a Reynolds equation with modified boundary conditions. While the agreement between the Gallis-Torcynzski model and the simulations performed in this work agree well for the larger gap sizes, there is significant discrepancy for the smaller gaps. This is largely due to the fact that the Gallis-Torcynzski model was developed based on simulations performed for a certain range of gap sizes and is not valid for very small gaps in the near-contact regime. The thin-beam model leads to significant over-prediction of the damping coefficient for all gap sizes because it assumes a linear dependence on the beam thickness. It can be clearly seen that the Gallis-Torcynzski model leads to infinite damping at very small gaps as opposed to simulations performed in this work which predict a finite damping even for a gap size of 50 nm. The previously published models were developed mostly for non-contacting beam oscillation dynamics and the comparison underlines the importance of correctly accounting for the conditions specific to near-contact damping occurring in the MEMS accelerometer.

The computed variation of the damping coefficient as a function of gap size was parametrized and applied in the beam dynamics simulations governed by Eq. (3). Note that a solution of 2D gas damping problem using the Boltzmann-ESBGK model takes from several hours to a few days. This is because of the large phase space that includes the two physical coordinates and two velocity coordinates, making the problem essentially four-dimensional. However, the resulting parametrized model that is formulated based on such simulations is semi-analytical and does not require any overhead in computational time when included in the beam dynamics simulations. The typical accelerometer beam dynamics simulations governed by Eq. (3) take only a few seconds of CPU time to be completed even for nanosecond-level resolution in time and submicron-level resolution in space.

The results of these simulations with the coupled inertia, bending and gas damping response have been compared with measurements of MEMS accelerometer beam closing and opening response done at various acceleration pulse profiles. The section below describes the comparison of modeling and experiments.

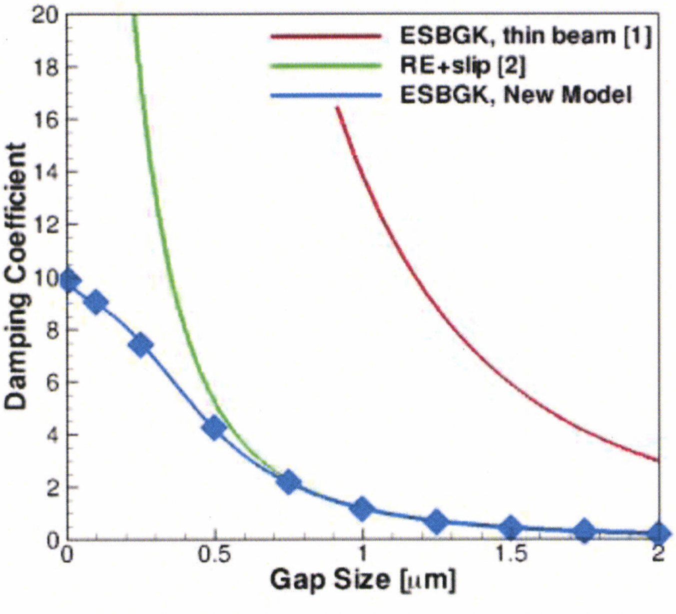

Figure 18: Comparison of gas damping coefficient obtained using ES-BGK simulations performed in this work with existing models.

2.2.4 *Validated Predictions*

In order to predict the opening and closing times of MEMS accelerometers for given dimensions and acceleration profiles, beam dynamics simulations were performed under a wide range of conditions. The predicted opening and closing times were then compared with those obtained from the experiments under different acceleration ramp rates and durations.

A typical acceleration profile used in experiments is shown in Figure 19 along with the measured voltage response. The contact was detected using the response voltage, which drops from about 5 V to nearly 0 V when a contact between the silicon beam and the SOI substrate occurs. For the acceleration profile shown in Figure 19, the first contact occurs at about 36 μs. One can notice that the contact is being discontinued and reestablished several times during the acceleration pulse. This is due to the beam bouncing from the hard SOI surface.

The beam dimensions used to compare the dynamic simulation predictions with measured closing and opening times were as follows: the length of L = 530 μm, the width of b = 68 μm, and the thickness of h = 20 μm. Here, the width (b) is an effective width of the beam which is used to account for the holes in the beam. The diameter of these holes is about 8 μm with four holes along the width of the beam. The holes are needed for the wider beams' release during the fabrication process but they also result in a reduced gas damping. The total width of the beam corresponding to the experiments with which the simulations are compared is about 100 μm and subtracting the width occupied by the holes leads to an effective width of 68 μm used in the simulations.

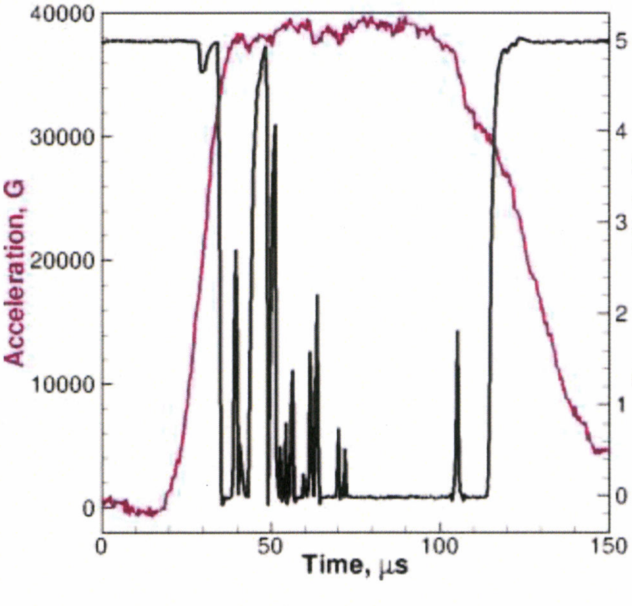

Figure 19: Acceleration profile and measured response for a typical experiment performed to characterize the MEMS accelerometers. Conditions correspond to experiment #12.

Results of beam dynamics simulations with the new near-contact damping model are shown in Figure 20. The conditions of these simulations correspond to the acceleration profile used in experiment #12 presented in Figure 19. The beam displacement profile and velocity variation along the length of the beam at four different instants of time before contact are plotted in Figure 20. The beam displacement profile at 20 μs shows that the beam is not altered from its initial position due to the low levels of acceleration. Most of the beam displacement over the 2 μm gap occurs between 20 μs and 36 μs (the instant at which the beam makes contact).

The beam bends because of the high external acceleration, reaching a maximum velocity at the tip at about 30 μs. *B*eyond this moment of time, the increase in gas damping due at the extremely small gap size leads to an overall deceleration of the beam tip. This can be observed by comparing the beam velocity at 30 μs and 35 μs. Figure 20 also shows the bending stress contours in the beam at different times. It can be seen that although the bending stress at the accelerometer beam anchor increases with increasing displacement, it remains quite low (< 30 MPa) even under this high g-load pulse.

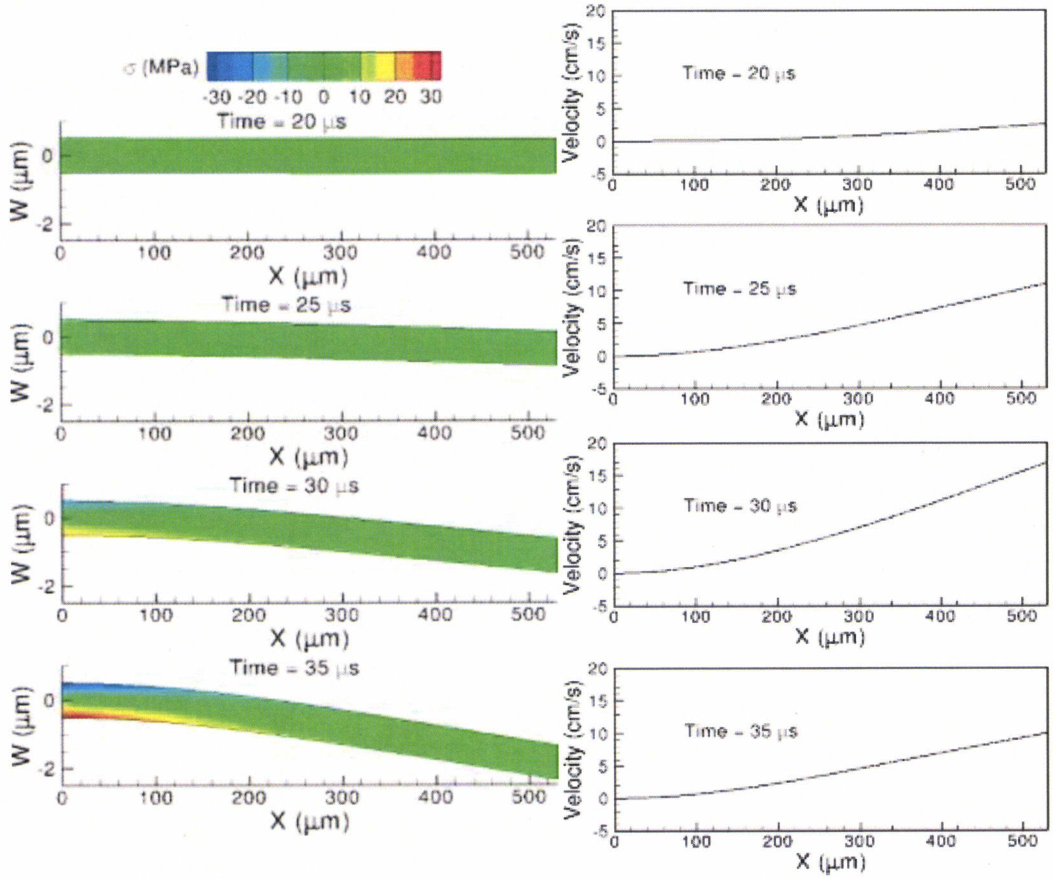

Figure 20: Beam displacement profiles (left) and velocity variation along length of the beam (right) at various instants of time before contact. Conditions correspond to experiment #12.

The opening and closing times predicted from the dynamics simulations using various damping models are compared with the measured contact times. Figure 21 compares the closing times and Figure 22 compares the opening times with the percentage errors for each damping model indicated next to each data point. The new model determined based on ES-BGK simulations performed in this work leads to very good agreement with the measured closing times.

The previous models of squeeze-film damping lead to over-prediction of the closing time due to over-prediction of the damping coefficient. The agreement for the opening times is good but there is some discrepancy for few of the experiments with the new model leading to an under-prediction by about 10%. However, the agreement in general is good when using the new damping model in the beam dynamics simulations. This comparison for contacting beam dynamics predicted by modeling with that measured by experiments under high-g accelerations present one of the first direct validation of physics-based modeling of contacting behavior of microscale structures.

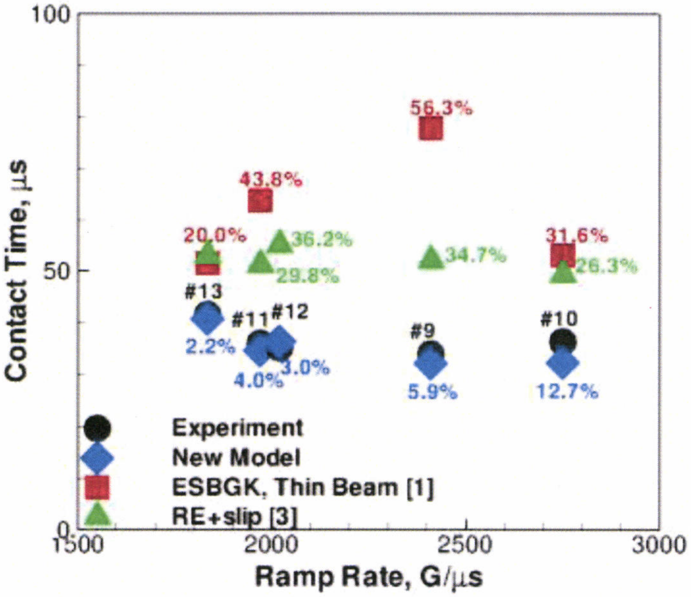

Figure 21: Comparison of measured and predicted (using various damping models) closing times for various experiments.

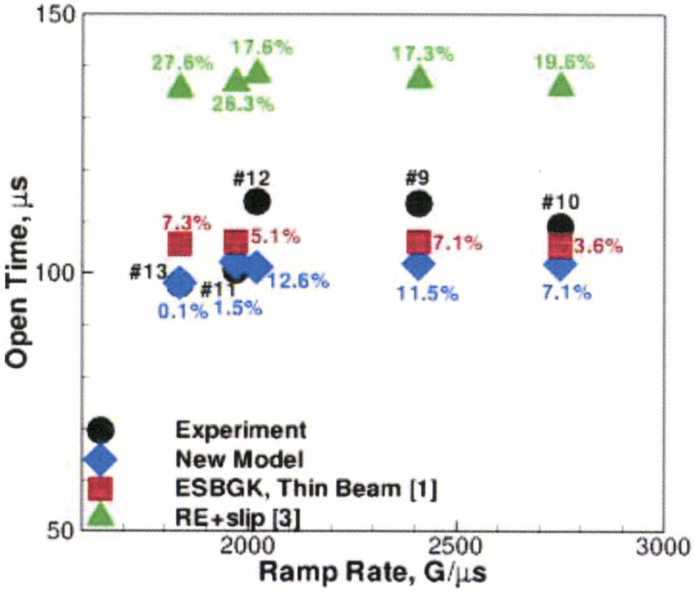

Figure 22: Comparison of measured and predicted (using various damping models) opening times for various experiments.

2.3 *Experimental Evaluation*

The experimental evaluation of the MEMS devices consists of the following steps 1) Packaging Process 2) Electrical Setup 3) Acceleration evaluation setup.

2.3.1 Packaging Process

In year 2, a suitable packaging process was developed to facilitate testing of the MEMS devices under shock loads. During packaging the fabricated die is placed in a ceramic leadless chip carrier (LCC) package and wirebonded. This is then hermetically sealed using a gold-indium bonding ring on a glass lid. This package was then soldered onto a PCB with the electrical wire in place as shown in Figure 11. The soldered package was then placed in a tungsten package and potted with an encapsulating material. The encapsulating material consists of Stycast 1090 SI cured with catalyst 11 in the ratios and temperatures indicated in the technical data sheet. This potting material helps to fix the positions of the components inside the tungsten package and thus reduces any unstable vibration on the device during impact testing as shown in Huang et. al [9].

2.3.2 Experimental Setup

Figure 23 shows the block diagram schematic of the electrical setup used for the measurement in the tests during years 2 & 3. In all experiments, five cantilevers of the same acceleration level are connected in parallel together and their combination is then connected through a resistor (R_s) to 5V power supply. The resistance (R_c) was then measured across the beam and the contact event.

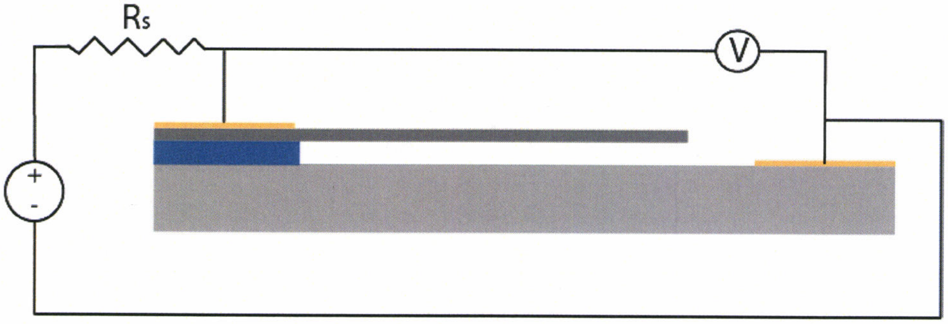

Figure 23: Schematic of the electrical setup

The packaged sample is connected to the electrical setup and subjected to impact accelerations using a modified Hopkinson bar setup (Figure 24). This acceleration setup uses the incident bar of a Hopkinson bar device. The acceleration levels are controlled by pulse-shaping techniques such that the packages attached to the end of the incident bar are subjected to accelerations with both amplitudes and durations actively controlled. The details of using a Hopkinson bars in impact experiments are described by a book by the PI [10].

2.3.3 Experimental Results

The fabricated devices were then loaded with the modified Hopkinson bar, which supplies constant levels of acceleration. The mechanical impact histories and the electric functions of the MEMS accelerometer were monitored in real time with high-speed digital oscilloscopes. The average resistance (R_c) measured during the acceleration events was then found to be ~3.23 kΩ. Figure 25 shows a characteristic response of an array of 40,000-g cantilevers with Rs = 510 Ω, which triggered at 44,960 g for a 140 μs applied acceleration profile with peak of 62,800 g. As evident from Figures 25 and 26, the device is shown to exhibit short duration responses after the acceleration has been turned off. These occur at regular intervals of 40 μs and can be attributed to contact bouncing resulted from impact-induced vibrations.

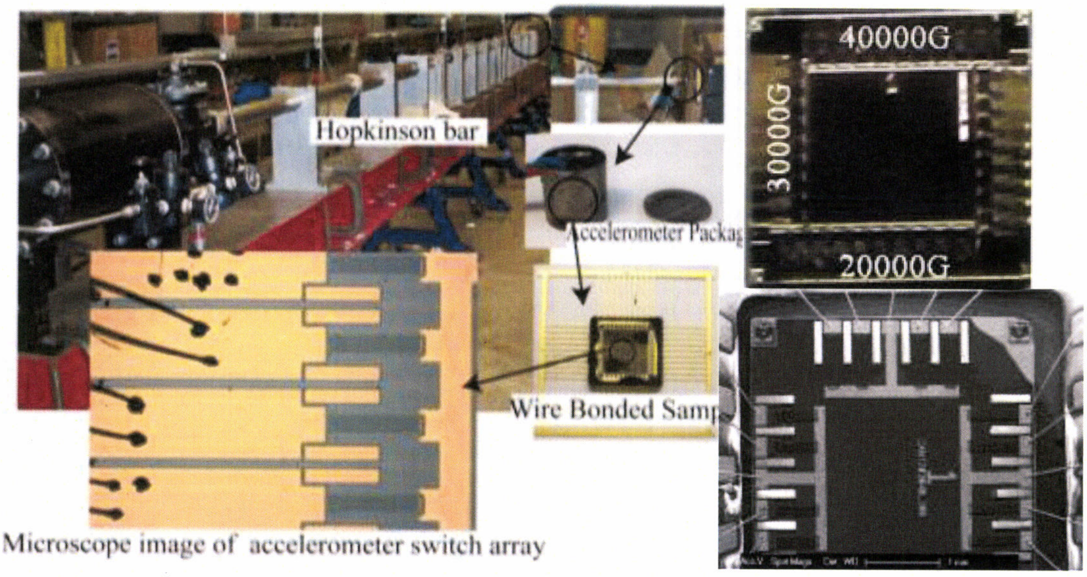

Microscope image of accelerometer switch array

Cantilever g switches dies

Figure 24: Packaging process and Hopkinson bar experimental setup

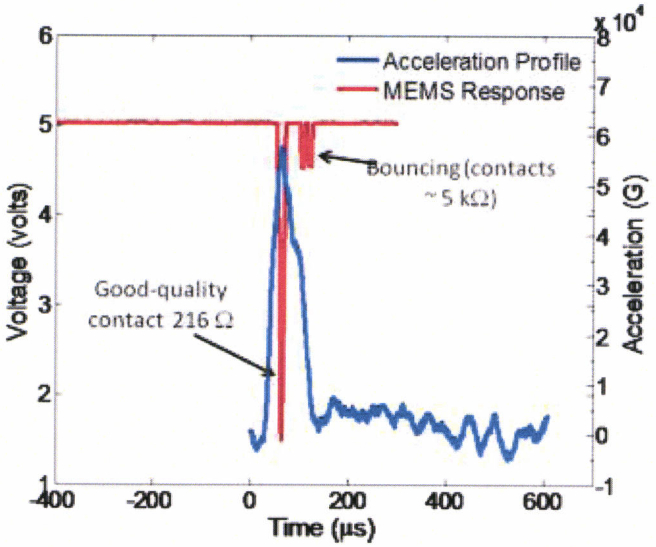

Figure 25: Parallel combination of five 40,000-g (530-µm long 100-µm wide) cantilevers triggering at 44,960 g for peak applied profile of 62,800 g

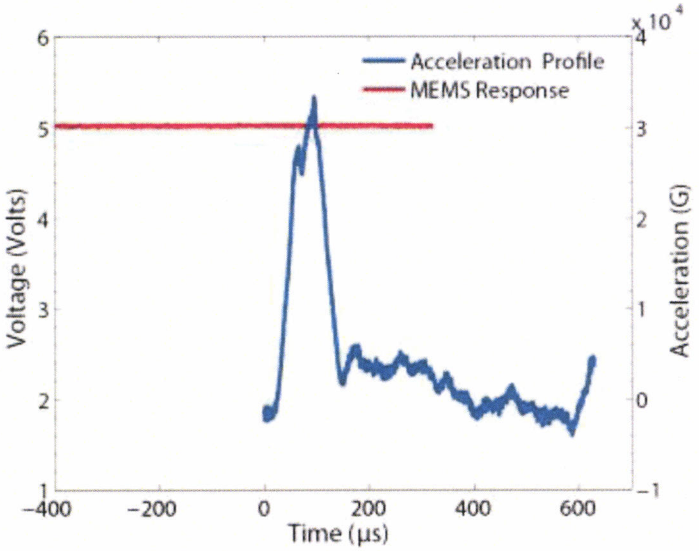

Figure 26: Parallel Combination of five 40,000-g (530-µm long 100-µm wide) cantilevers under lower acceleration conditions of 33,420 g

Figure 27 shows the parallel combination of 20,000-g (630-µm long 100-µm wide) cantilevers triggering at 15,000 g for a peak applied profile of 24,000 g. The substrate resistivity was increased in this test to alleviate signal coupling effects. As evident in the results, there is an indication of bouncing and some adhesions issues when contact occurs. Additional tests results are also available in Appendix A. In all the applied tests, we can see that devices successfully detect the acceleration within 1,000-5,000 g of their designed level. The variations between the designed and measured acceleration levels can be attributed to the approximations used in the design equations and the fabrication non-idealities especially at the anchor. In order to improve on the accelerometer design, a new prediction model was designed using gas flow dynamics, which is explained in section 2.2.

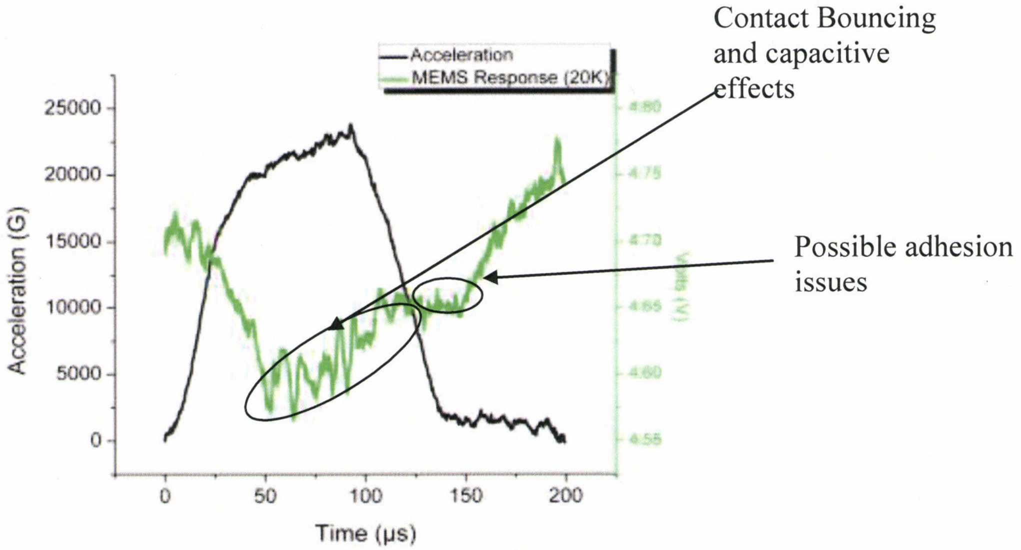

Figure 27: Parallel Combination of five 20,000-g (630um long 100-um wide) cantilevers triggering at 15,000 g for peak applied profile of 24,000 g

In order to evaluate redundancy performance, tests were conducted with different dies containing ten cantilevers, five cantilevers, and a single cantilever of the same acceleration level are connected in parallel subjected to acceleration loads. Figure 28 shows a parallel combination of ten 40,000–g triggering at 37,273 g. These results show that increasing the number of devices significantly increases the contact bouncing experienced, but significantly decreases the measured contact resistance when compared to dies containing five cantilever connected in parallel. In addition, a high degree of failure was also seen in dies containing single beams of a particular acceleration level caused due to fabrication and packaging. As a result of this no acceleration measurement were available to present from single devices, but this in turn confirms the need for redundancy. The observations reveal that in order to optimally detect and reliably measure acceleration, i.e. less contact bouncing in the response, five cantilevers were found to be the most suitable number needed for each level. Additional research and testing is needed in this area to better quantify these results.

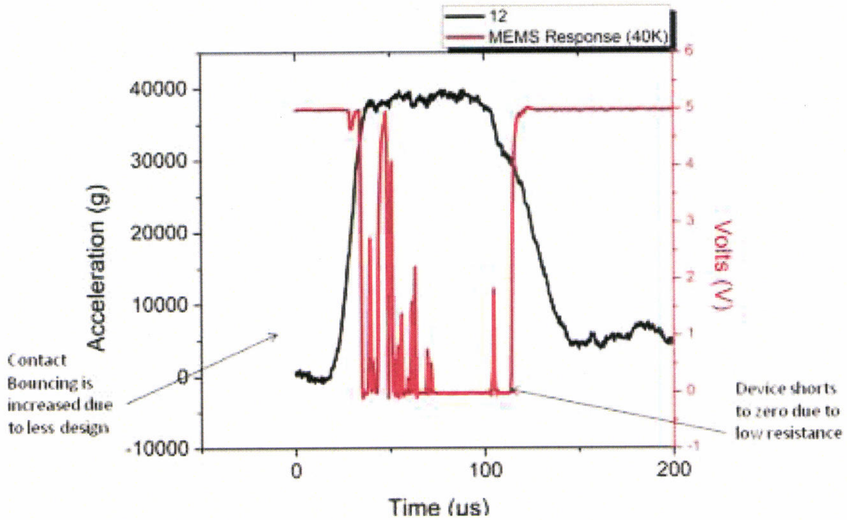

Figure 28: Parallel Combination of ten 40,000-g (530-µm long 100-µm wide) cantilevers triggering at 37,273 g.

2.4 *Real-time Contact Monitoring with Ultra-low-power Electronics*

2.4.1 Experimentally Identifying Bouncing Behavior: Single Crystal Silicon Switch

As evident from the previous results, there is a clear presence of bouncing in these devices. Consequently, it is necessary to carefully monitor in real time the dynamic behavior of the device under testing. In order to do so we designed a contact monitoring circuit (described in more detail below) and tested its performance on an electrostatically actuated switch built with a similar fabrication process and materials [11]. The switch consists of a 2-μm thick single-crystal silicon cantilever beam and a 2-μm thick gold biasing electrode. The contact areas are suspended approximately 2.5 μm above the silicon cantilever beam. The switch is fabricated in the normally open (off state). The fabrication process is summarized in Figure 29 and is outlined as follows: Beginning with a bare SOl wafer (A) and using standard positive photolithography techniques, the device layer is patterned and reactive ion etched using SF_6 plasma. This is followed by depositing and patterning the RF contact on the device (B). Using positive resist, the sacrificial layer is patterned and baked (C) and the signal lines and biasing structure is deposited and anchored to isolated islands of the device layer (D). A hot positive resist stripper release (E) is followed by a HF dip to etch the buried oxide layer and release the device layer (F) before drying. The process requires 5 masks in total. A representative device is shown in Figure 30.

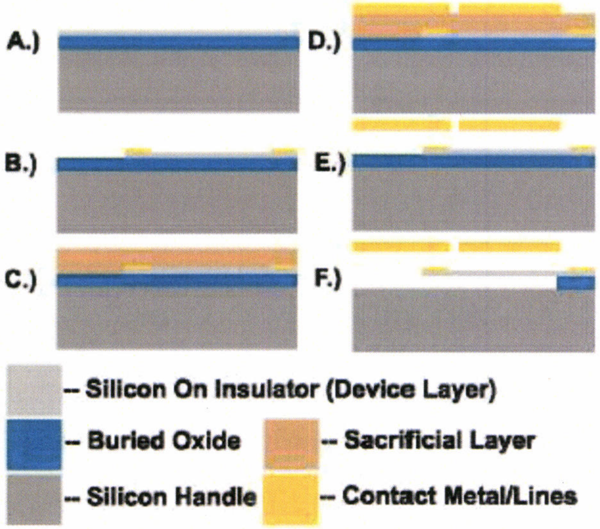

Figure 29: Fabrication of electrostatically actuated single crystal silicon switch

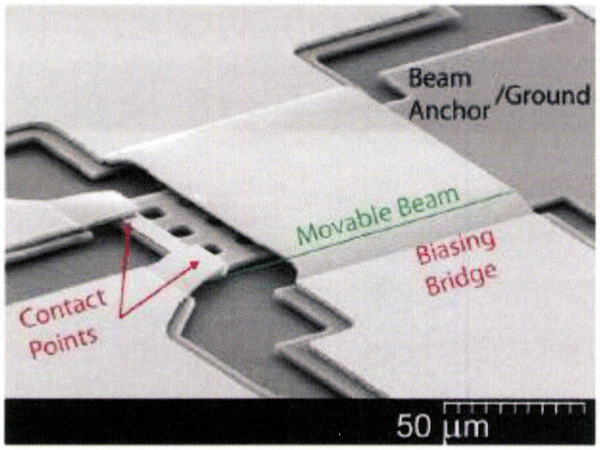

Figure 30: SEM image of a representative single crystal MEMS switch under study

2.4.2 Capacitive Dynamic Measurement:

The system diagram for the capacitive measurement circuit is shown in Figure 31. The semi-digital readout circuit acts as capacitance to pulse-width-modulated signal (PWM) block (Figure 31) [12]. The pulse width varies as a function of the RC time constant. The resistance is a fixed and known value, and the capacitance increases as the switch closes. As a result, the circuit is inherently linear. Due to the digital nature of the circuit, the output can be directly connected to a microprocessor to collect data in real-time. Low power self-tuning comparators are used to compare the input voltage with the supply voltage, $V_{DD}/2$. As long as the voltage across the capacitance is less than this value, the output of the sensor interface circuit is high. The voltage across the capacitor *(Va)* can be determined as shown in Eq. (7) [12].

$$V_c = V_{DD}e^{-t/RC} \qquad (7)$$

The time T required for Vc to reach $V_{DD}/2$, [10] can be found from Eq. (8) [12] and is shown to be

$$T = RC\ln(2) \qquad (8)$$

It can be seen that timing differences as measured by the circuit are linearly dependent on the measured capacitance changes. As such, the circuit's readout is independent of parasitic or reference capacitances. In order to eliminate any DC offset due to charge buildup over time, the transistor connected in parallel with the sensed capacitance is used to reset the voltage across the capacitor [13].

The maximum capacitance that can be read is limited by the clock high time (T_{HIGH}) and clock low time (T_{LOW}) [12]. Mathematically, this is represented in Eqns. 9 and 10 [12].

$$C_{MAX} = \frac{T_{HIGH}}{R\ln(2)} \qquad (9)$$

$$C_{MIN} = \frac{T_{LOW}}{5(r_{ON}\|R)} \qquad (10)$$

Where r_{on} is the transistor's on resistance. The factor 5 in Eq. 10 is a result of requiring 5 time constants for the capacitor to be assumed to be completely discharged. The minimum of these two factors set the bottleneck for the maximum capacitance that can be measured. The minimum detectable capacitance is determined primarily by the jitter at the output [12]. The measured capacitances in this experiment are much greater than the circuit's threshold for minimum detectable capacitance.

Power consumption in the circuit was measured to be 60 µW with a reference resistance of 2.7 MΩ and a reference capacitance of 1 pF at an operating frequency of 32.768 kHz [12]. The operating frequency is determined by a clock input. A crystal oscillator is commonly used to reduce jitter, though for experimental purposes a function generator was used in this work. While the power consumption of the clock source in non-negligible, in a system implementation it is often amortized across the entire system.

2.4.3 Measurement Results: Capacitance Sensing

To obtain the electronic measurements, the silicon switch is connected to the circuit as shown in Figure 31. Figure 32 shows the raw output of the circuit and a biasing waveform synchronized in time. While the bias is at zero potential, the gap is at its maximum value and thus the capacitance at the contact in the off state is at its minimum value of approximately 1 fF. The resulting output pulse width is approximately 50% duty cycle. Upon actuation, the beam moves toward the contact and the capacitance increases, resulting in an increase in the duty cycle until contact. This transition between low and high duty cycles occurs several times during a switching event as the beam bounces up repeatedly. When the beam settles in the closed state and remains in contact the duty cycle is constant at 80%. These values are a product of the crystal oscillator. The approximately 50% minimum duty cycle is due to the reading of parasitics of the circuit and setup. 80% duty cycle is the duty cycle of the clock and cannot be exceeded. The measurement shows landings of finite duration in the µs range

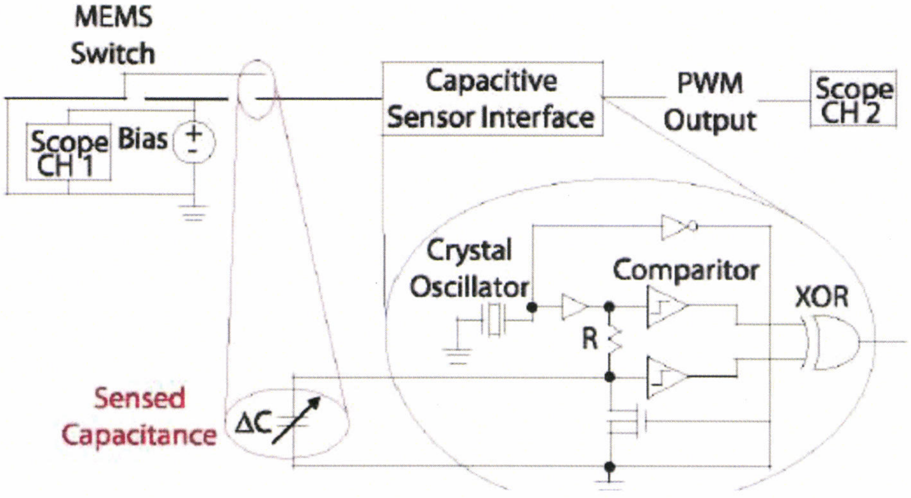

Figure 31: Block Diagram schematic of the measurement circuit

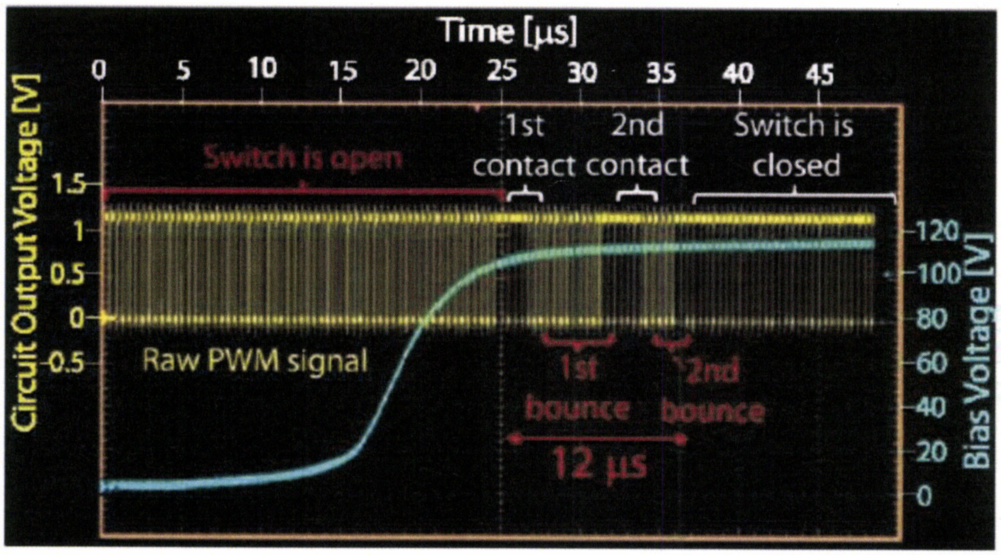

Figure 32: Raw output of the measurement circuit with respect to the biasing waveform

2.4.4 Resistive Dynamic Measurement

In order to examine the potential degradation of the contact, the capacitive measurement circuit was modified. The output duty cycle now varies with change in RC time constant and is now based on a reference capacitor (C_{ref}) and the target resistance. Due to the inherently linear and digital output, the circuit is well suited for real-time data monitoring via a direct feedthrough to a microprocessor.

The experimental setup and a simplified circuit diagram are shown in Figure 21. The maximum measureable resistance is limited by the high time (T_{HIGH}) of the clock and the low time (T_{low}) of the clock [12] which can be derived from equations 3 & 4.

For the purposes of this experiment, a crystal oscillator and battery were used to reduce jitter at the output. Here, the resolution was limited by (a) the jitter and (b) the series resistances shown in Figure 33. These resistances are necessary for current limiting and improving RF isolation of the circuit. With these limitations, the minimum detectable resistance is approximately 100 Ω. This also defines the measurement resolution. On the other hand, the maximum measurable resistance was approximately 2.6 kΩ. While the minimum detectable resistance may seem large compared to a typical on-state resistance of ~ 1 Ω, we are still able to accurately detect the closed and open positions of the switch due to the relatively large dynamic range of the circuit. Further improvements of the measurement technique may enable the accurate calculation of the on-state contact resistance. However, for the purposes of this study, the on/ off resistance contrast is sufficiently high.

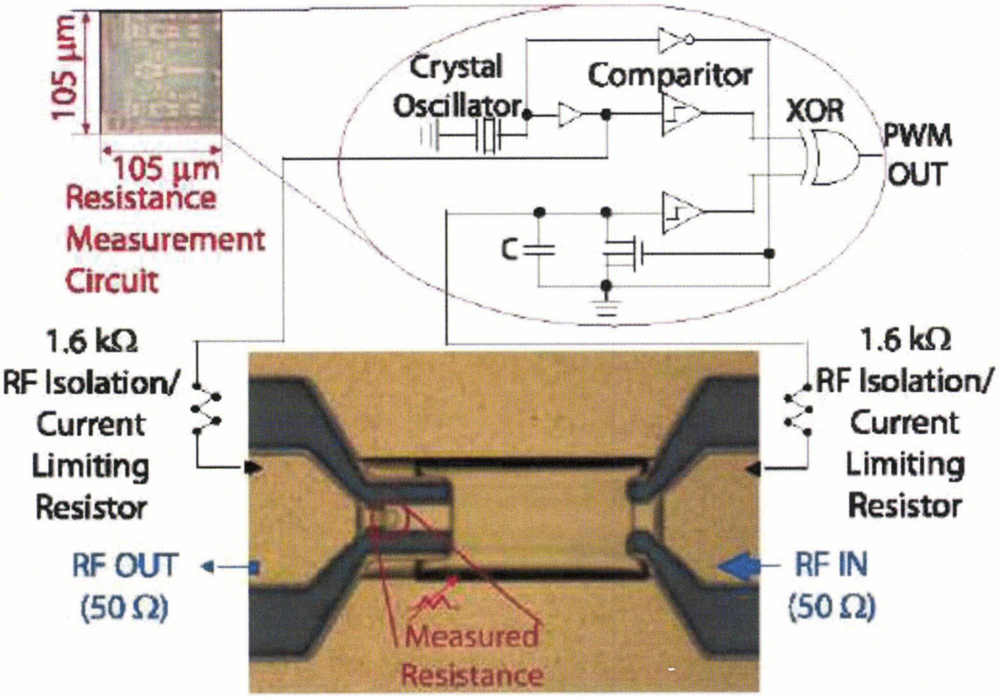

Figure 33: Setup of the resistive monitoring circuit

Power consumption has been measured as low as 60 μW operating at 32 kHz [14]. For this experiment, it was operated at 4 MHz and simulations indicate the power draw is approximately 180 μW at this frequency.

2.4.5 Measurement Results: Resistance Sensing

Figure 34 shows a sample of the raw pulse width modulated output of the sensing circuit with a. bias waveform overlayed and synchronized in time. For validation, the measurement was compared to bounces that could be detected by an oscilloscope with a low voltage applied to the switch output (Figure 35). The small variations (on the order of a few hundreds of nanoseconds) between the measurements are attributed to slight variations in the switch cycling trials as well as the sampling of the sensing circuit occurring every 250 ns. The results were further validated by the state-of the-art measurement technique for unpackaged devices, the laser doppler vibrometer (LDV). The monitoring technique presented is capable of operating at the same frequency with the LDV with synchronized triggering. By acquiring simultaneous measurements it will be possible to assess any sources of error in the electronic measurement to refine the technique. An additional capability of the circuit is the ability to observe the impact of cold switching and minute amounts of current on bounce behavior.

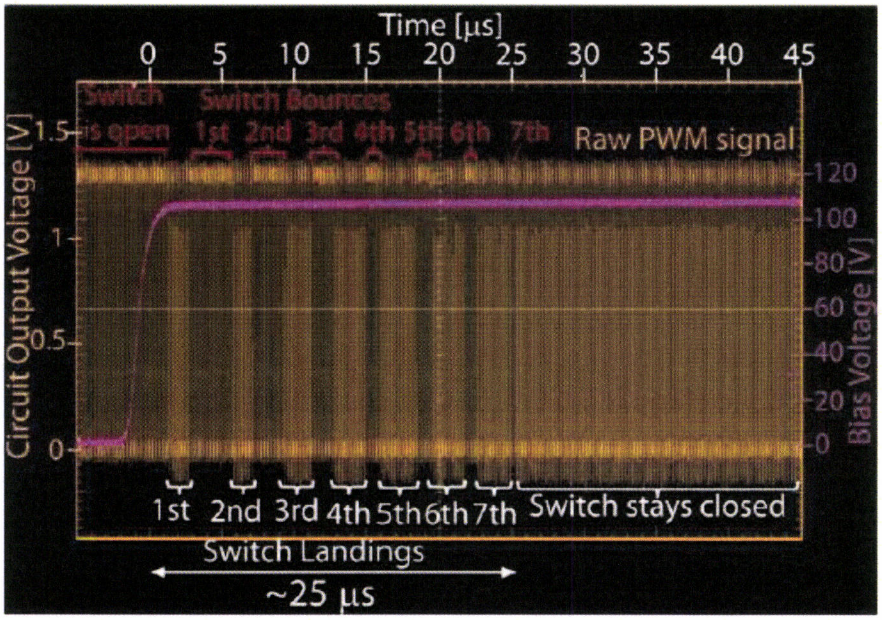

Figure 34: Raw output of the measurement circuit showing switch bouncing

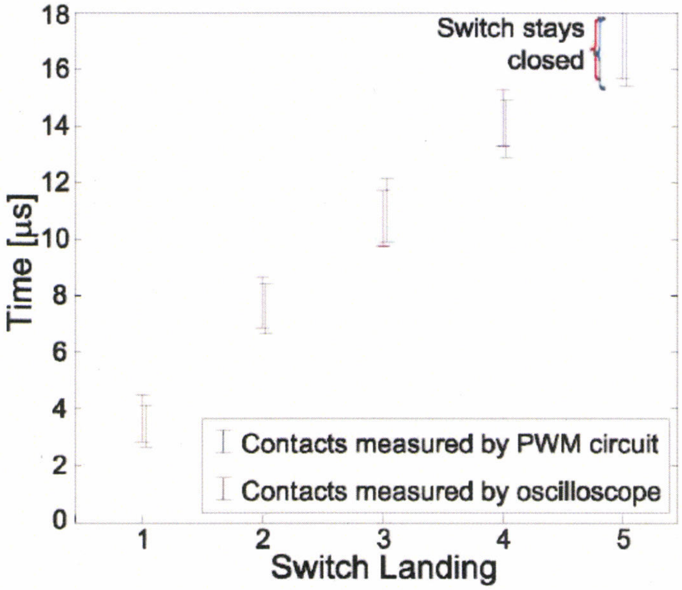

Figure 35: Comparison of switch landing as measured by resistive PWM readout circuit and voltage divider connected to an oscilloscope

As can be seen in Figure 36 it is possible to extract height information from the PWM data output by the capacitive sensing circuit, even with only 10% resolution when as much as 40% can be achieved. With external validation, it will be possible to correlate the circuits readout to actual bounce height. Figure 37 shows that the electronic technique shows excellent correspondence with simultaneous measurements from the LDV.

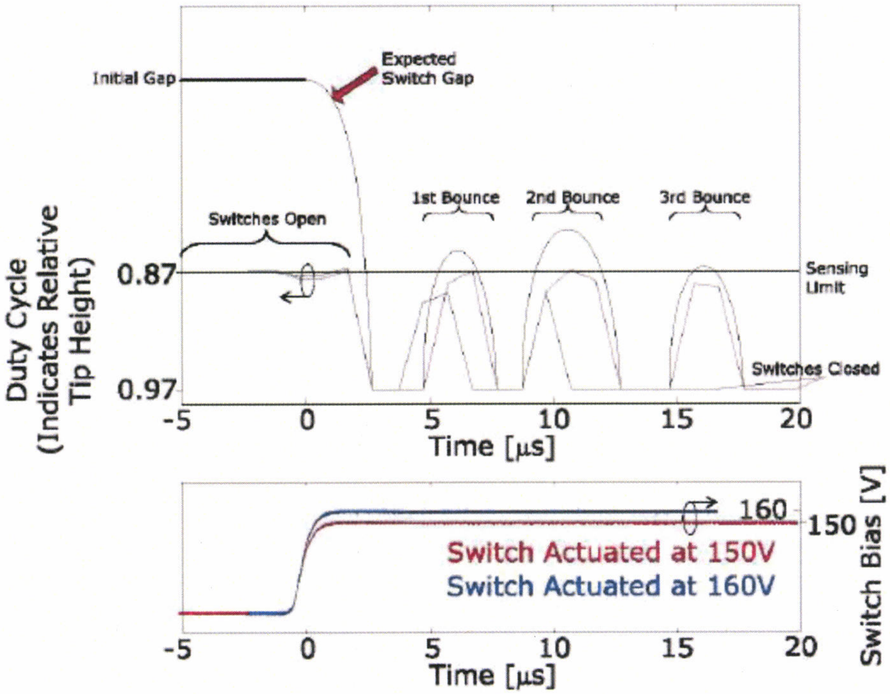

Figure 36: PWM duty cycle during bouncing events

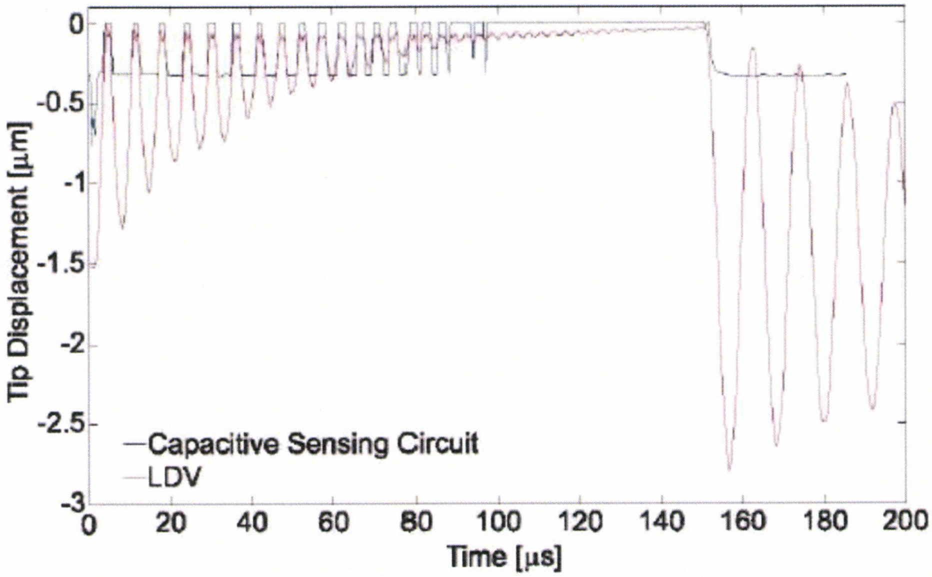

Figure 37: Time synchronized plot of LDV signal and PWM output from capacitive sensing circuit

Thus from the above results we can see the contact monitoring circuit has been successfully validated.

2.4.6 Measured Results for the MEMS Accelerometers

With the successful validation of the contact monitoring, the packaged MEMS device was then connected to the capacitive bounce measurement circuit via the system diagram shown in Figure 38. This is then subjected to the acceleration test using the Hopkinson bar.

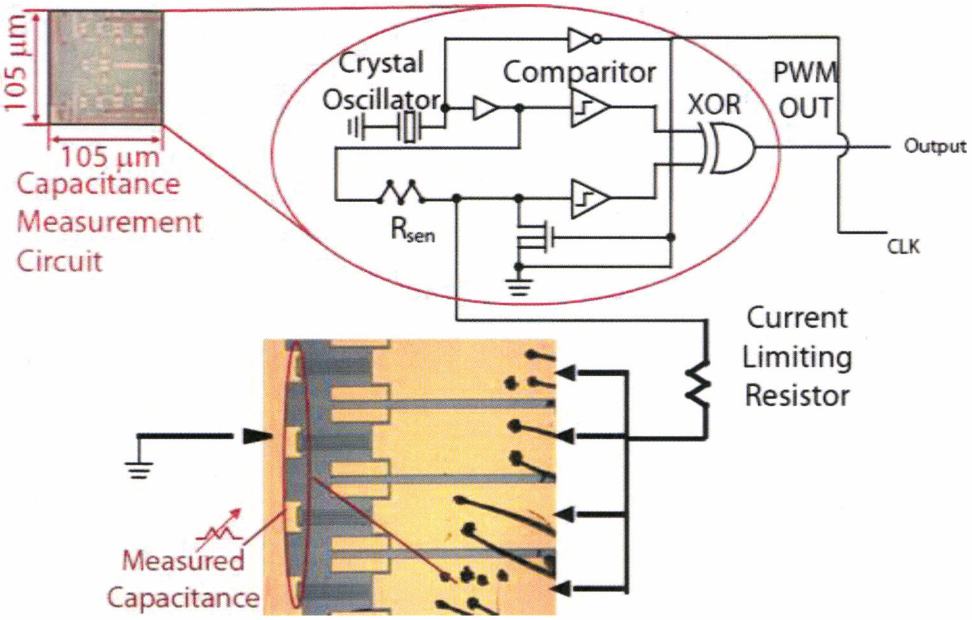

Figure 38: Schematic of the accelerometer connected to the capacitive measurement circuit

Figure 39 shows a raw response of the MEMS device for a peak applied profile of 55,000 g. The inset in Figure 39 shows the presence of bouncing in the device response indicated by the partial pulse width response. Using the aforementioned equations in the capacitive measurement section, the capacitance change in the device is extracted and plotted versus acceleration below. This capacitance change as mentioned above corresponds to the change in gap of the device. This is shown in Figure 40. This graph shows a set of 40,000 g beams triggering at 40,780 g for a peak applied profile of 55,000 g. We can see the capacitance varying from 0.15 nF to 1 nF, which in turn corresponds to an approximate gap change of 0.5 µm to 10 nm. However, as mentioned in the above section, the low level gap measurement is limited by the parasitic in the cables used in the measurement which leads to an a baseline measurement of 0.15nF in the capacitance.

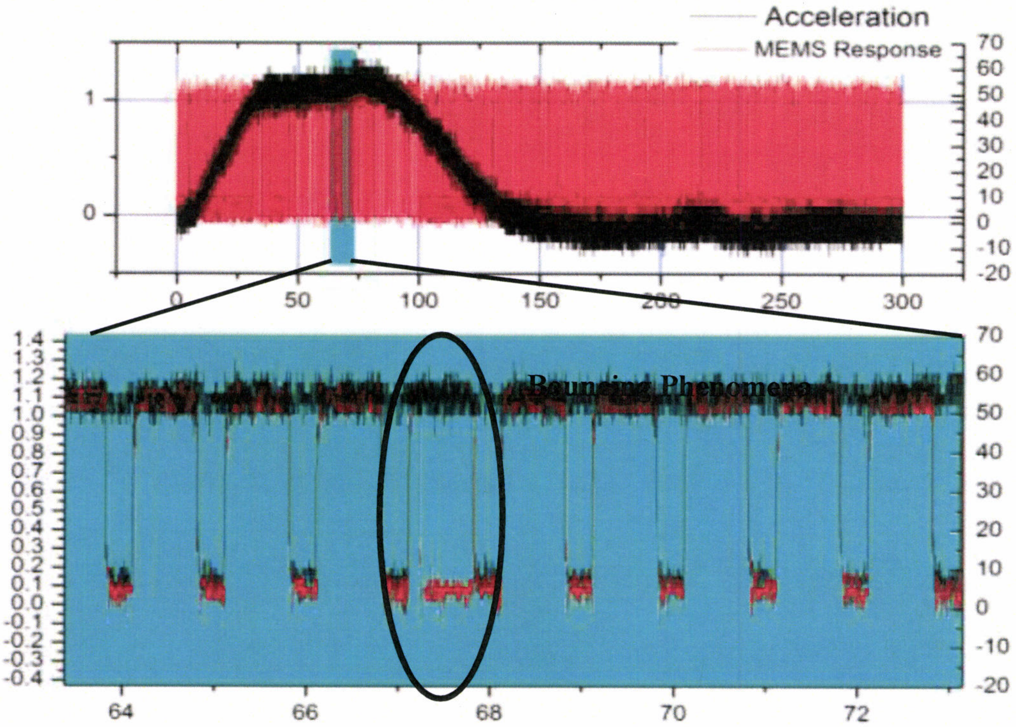

Figure 39: Raw response of the circuit for a applied acceleration profile of 55,000 g

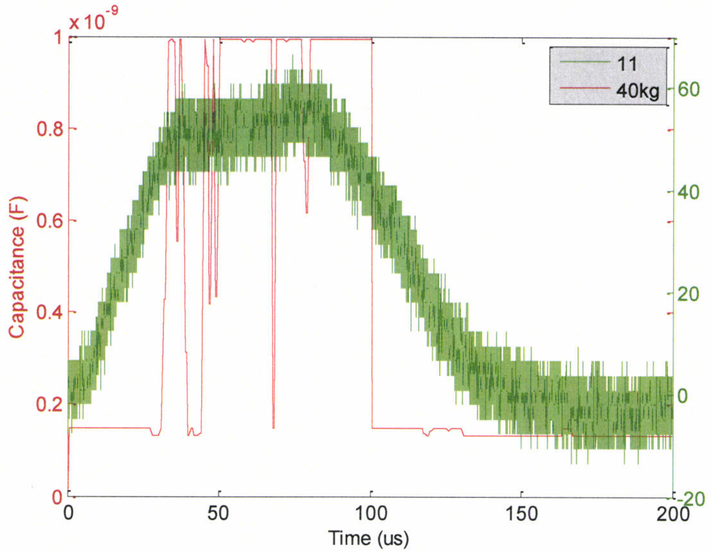

Figure 40: Capacitive response data of 40000-g beams for an applied acceleration profile of 55,000 g

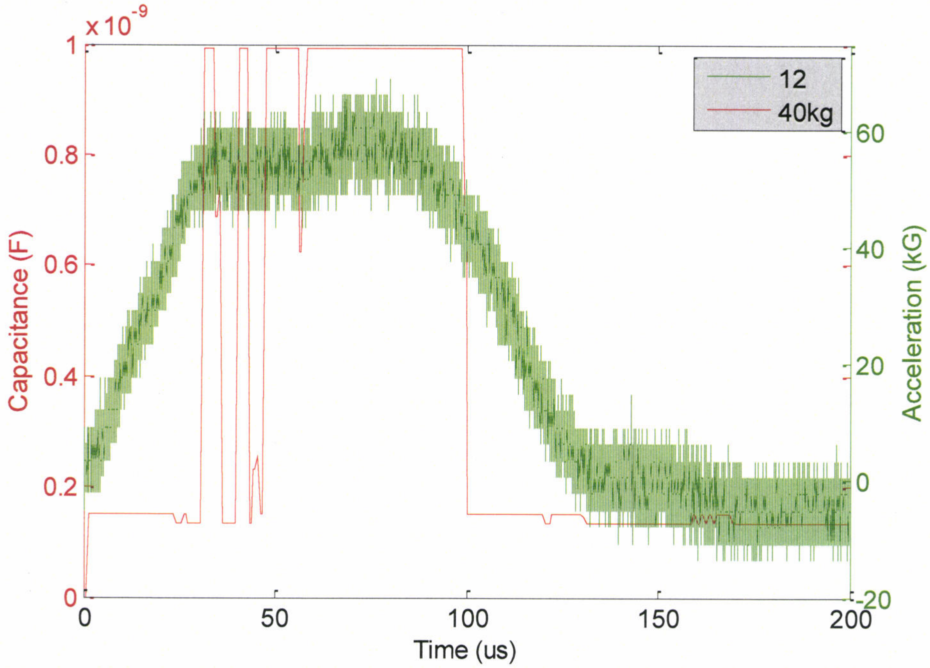

Figure 41: Capacitive response data of 40000-g beams for an applied acceleration profile of 66,000 g

Figure 41 shows the response of similar devices for a higher applied profile of 66,000 g triggering at 43,000 g. This figure indicates a clear reduction in the bouncing phenomena as the acceleration level increases. These results show a clear evidence of detection of acceleration and the presence of bouncing thus validating the previous experimental results. Further work needs to be conducted by varying the reference resistor and the frequency of the clock signal, in order to increase the dynamic detection range of the circuit for the MEMS devices.

2.5 *Concluding Remarks*

In this study we have successfully demonstrated the first proof-of-concept devices for detecting high-g events using digital MEMS accelerometers based on electronic detection of silicon-silicon contacts. These contacts are explored for the first time. Our measurements indicate that they can reliably result in on-resistance values of ~3 kΩ. Our designs have successfully detected three different acceleration levels in a single direction up to 45,000 g. Redundancy of the device was also explored, with the conclusion being at least 5 sensors per acceleration level are needed for reliable detection. In addition, a first low-power sensor interface for in-situ monitoring of MEMS device was developed. Successful electronic monitoring of contact and bouncing events were demonstrated and validated using a characteristic silicon switch. These results were successfully validated using a laser doppler vibrometer (LDV). This enables a real time monitoring of dynamic and contact behavior of packaged MEMS devices. The capacitive monitoring circuit was successfully interfaced with the MEMS g-switches. Preliminary results have shown the presence of bouncing and dynamic movement of the cantilevers under high-g loads using the monitoring circuit.

2.6 *Possible Future Directions*

- The detection range of the bounce measurement circuit is limited by the presence of parasitic and hence further monitoring experiments under high-g loads need to be preformed.
- Future work on contact degradation both theoretically and experimentally under high-g loads needs to be performed in order to successfully model the contact behavior of the devices.
- Theoretical exploration of contact and structural degradation can be accomplished by researching the impact of stress-induced waves on the structure during high-g loads.
- Contact degradation can be explored experimentally by integrating the MEMS device with the resistive monitoring circuit via the schematic shown in Figure 42.
- Further work needs to be performed to create a full-fledged measurement system for detection of multiple levels simultaneously.

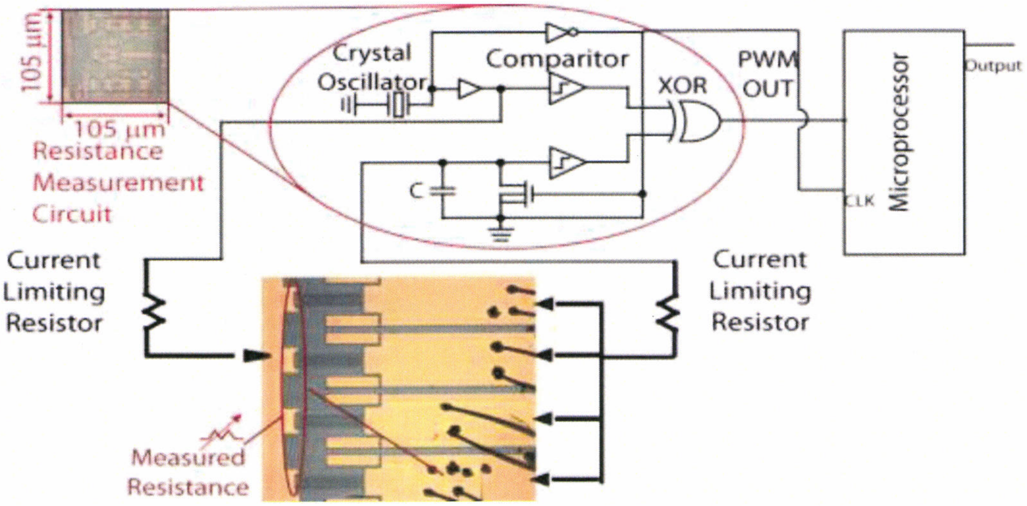

Figure 42: Schematic of the accelerometer connected to the capacitive measurement circuit

3. References

[1] B. R. Davies ,S. Montague , V.I. Bateman, F.A. Brown, R. Chanchani , T. Christenson, J. Murray, D. Rey, D. Ryerson "High-G Accelerometer for Earth-Penetrator Weapons Applications LDRD Final Report" Sandia National Labratories, NM, Tech. Rep. SAND–98-0510, Mar.1998.

[2] Beliveau, A.; Spencer, G.T.; Thomas, K.A.; Roberson, S.L.; , "Evaluation of MEMS capacitive accelerometers," *Design & Test of Computers, IEEE* , vol.16, no.4, pp.48-56, Oct-Dec. 1999

[3] V. Bateman, N. Davie, and F. Brown, "Characteristics of a piezoresistive accelerometers in shock environments up to 150,000g," in *Institute of Environmental Sciences Proceedings*, Feb. 1995, pp. 290–294.

[4] T. Togami, V. Bateman, and F. Brown, "Evaluation of a hopkinson bar fly-away technique for high amplitude shock calibration accelerometers," Sandia National Labratories, NM, Tech. Rep. SAND–98-1444C, Nov.1988.

[5] V. Srikar and S. Senturia, "The reliability of microelectromechanical systems (MEMS) in shock environments," *Microelectromechanical Systems, Journal of*, vol. 11, no. 3, pp. 206 –214, June 2002.

[6] J. Kimberley, I. Chasiotis, and J. Lambros, "Failure of microelectromechanical systems subjected to impulse loads," *International Journal of Solids and Structures*, vol. 45, no. 2, pp. 497 – 512, 2008.

[7] D. V.-K. et. al., "Anelastic creep phenomena in thin metal plated cantilevers for mems," *Materials Science of MEMS Devices,* vol. 657, pp. EE2.5.1-2.5.6, 2001.

[8] G. Rebeiz, *RF MEMS, Theory, Design and Technology*. John Wiley and Sons, 2003.

[9]W. Huang, X. Cai, B. Xu, L. Luo, X. Li, and Z. Cheng, "Packaging effects on the performances of MEMS for high-g accelerometer with double-cantilevers," *Sensors and Actuators A: Physical*, vol. 102, no. 3, pp. 268 – 278, 2003.

[10] Chen, W., and Song, B., 2010, Split Hopkinson (Kolsky) Bar: Design, Testing, and Applications, Springer (388 pages).

[11] Fruehling, A.; Pimpinella, R.; Nordin, R.; Peroulis, D.; , "A single-crystal silicon DC-40 GHz RF MEMS switch," *Microwave Symposium Digest, 2009. MTT '09. IEEE MTT-S International* , vol., no., pp.1633-1636, 7-12 June 2009

[12] J. Lu, M. Inerowicz, S. Joo, J.-K. Kwon, and B. Jung, "A low-power, wide dynamic range semi-digital universal sensor readout circuit using pulse-width modulation," *IEEE Sensors Journal, 2010.*

[13] M. A. Khater, "Master's Thesis, Purdue University," August 2009.

[14] A.A. Alexeenko, S.F. Gimelshein, E.P. Muntz, A.D. Ketsdever, "Kinetic Modeling of Temperature-Driven Flows in Short Microchannels," International Journal of Thermal Sciences, Vol. 45, No. 11, Nov. 2006, pp. 1045-1051.

[15] X. Guo and A. Alexeenko, "Compact Model of Squeeze-Film Damping based on Rarefied Flow Simulations," Journal of Micromechanics and Microengineering, Vol. 19, No. 4, April 2009, 045026.

[16] M. A. Gallis M A and J. R. Torczynski, "An Improved Reynolds-equation Model for Gas Damping of Microbeam Motion", IEEE/ASME Journal of Microelectromechanical Systems, Vol. 13, pp. 653–659, 2004.

4. Publications from This Project

Fruehling, A.; Abu Khater, M.; Byunghoo Jung; Peroulis, D.; , "CMOS-based monitoring of contact events up to 4 MHz in ohmic RF MEMS switches," Microwave Symposium Digest (MTT), 2010 IEEE MTT-S International, pp.300-303, 23-28 May 2010.

Fruehling, A.; Abu Khater, M.; Byunghoo Jung; Peroulis, D.; , "Real-time monitoring of contact behavior of RF MEMS switches with a very low power CMOS capacitive sensor interface," *Micro Electro Mechanical Systems (MEMS), 2010 IEEE 23rd International Conference on* , pp.775-778, 24-28 Jan. 2010.

Parkos, D.; Raghunathan, N.; Ayyaswamy, V.; Alexeenko, A.; Peroulis, D.; , "Near-contact damping model and dynamic response of μ-beams under high-g loads," *Micro Electro Mechanical Systems (MEMS), 2011 IEEE 24th International Conference on* , pp.465-468, 23-27 Jan. 2011.

N. Raghunathan, E. Nishida, A. Fruehling, W. Chen, and D. Peroulis. "Arrays of silicon Cantilevers for detecting high-g rapidly varying acceleration profiles". In *Sensors, 2010 IEEE,* Nov. 2010.

Parkos, D.; Raghunathan, N.; Ayyaswamy, V.; Alexeenko, A.; Peroulis, D.; , "Near-contact damping model and dynamic response of μ-beams under high-g loads," *IOP science Journal of Micormechanics and Microengineering,* Paper under preparation.

D. Peroulis, W. Chen, N. Raghunathan, and A. Fruehling, "A novel MEMS digital accelerometer," *IEEE/ASME Journal of MEMS,* Paper under preparation.

Raghunathan, N; Sanborn, B; Chen,W; Byunghoo Jung; Peroulis, D.; , "Real-time monitoring of contact behavior of High –G switches under dynamic High-G loads," *Micro Electro Mechanical Systems (MEMS), 2011 IEEE 24th International Conference on* , Paper under preparation

Raghunathan, N; Yang, Z; Peroulis, D.; , "Resistance characterization of Silicon- Silicon Contacts ," *Micro Electro Mechanical Systems (MEMS), 2011 IEEE 24th International Conference on* , Paper under preparation

5. Appendix A

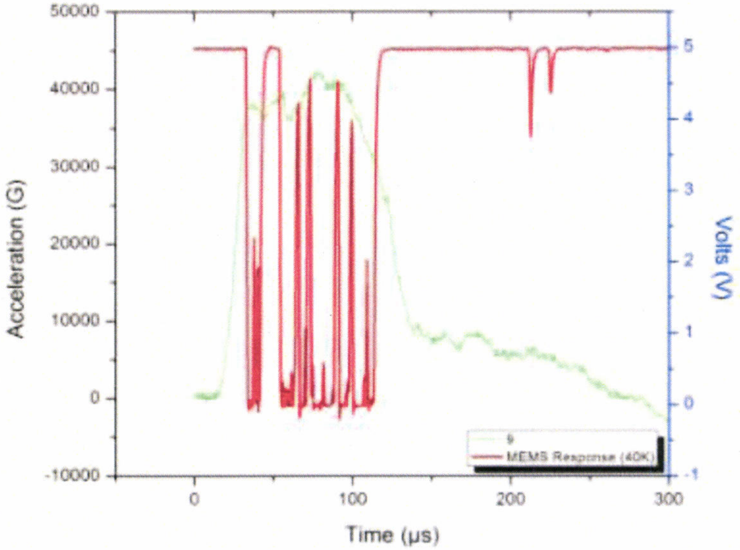

Figure 1: Parallel combination of ten 40,000-g (530-µm long 100-µm wide) cantilevers triggering at 37,386 g

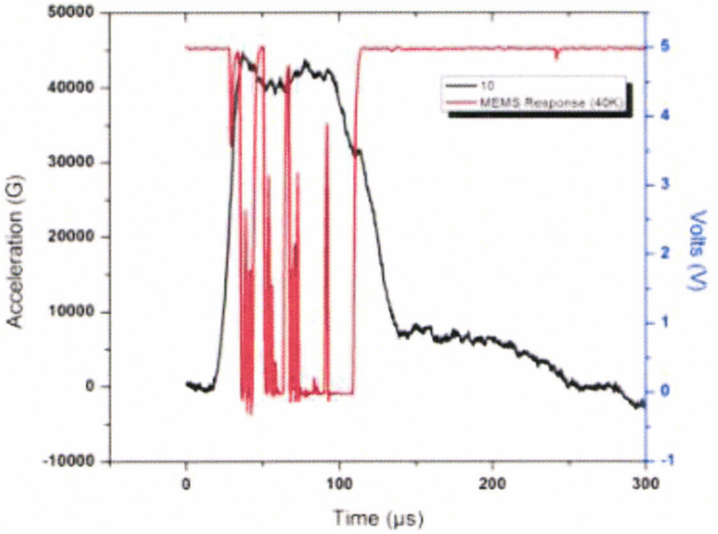

Figure 2: Parallel combination of ten 40,000-g (530-µm long 100-µm wide) cantilevers triggering at 38,443 g

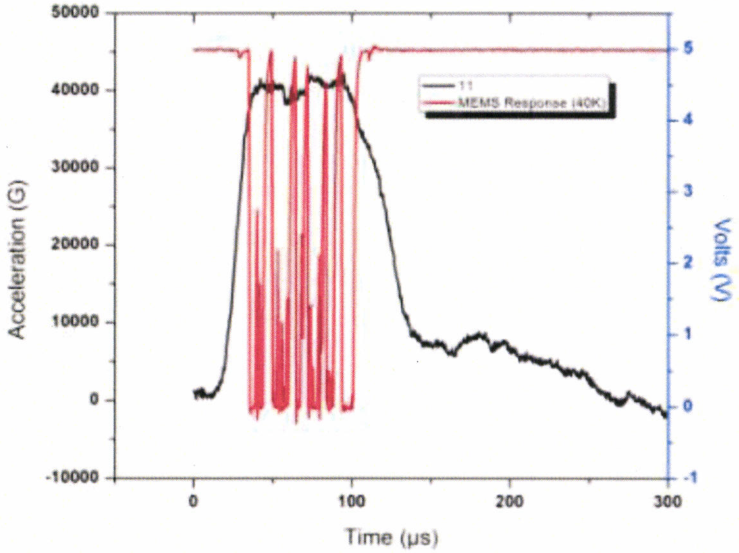

Figure 3: Parallel combination of ten 40,000-g (530-µm long 100-µm wide) cantilevers triggering at 38,443 g

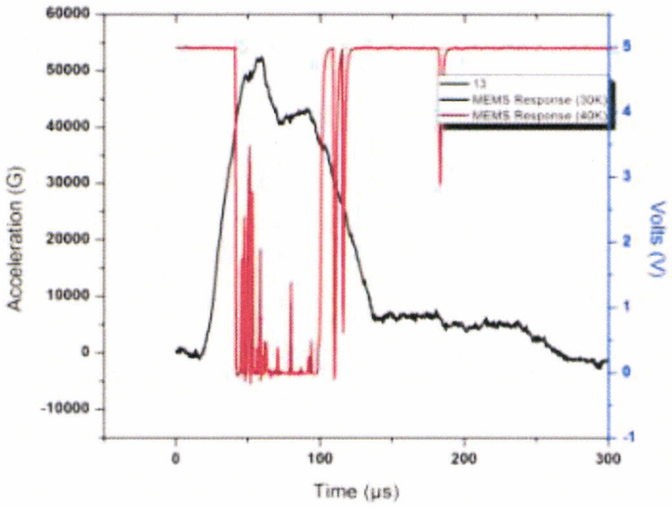

Figure 4: Parallel combination of ten 40,000-g (530-µm long 100-µm wide) cantilevers triggering at 38,624 g

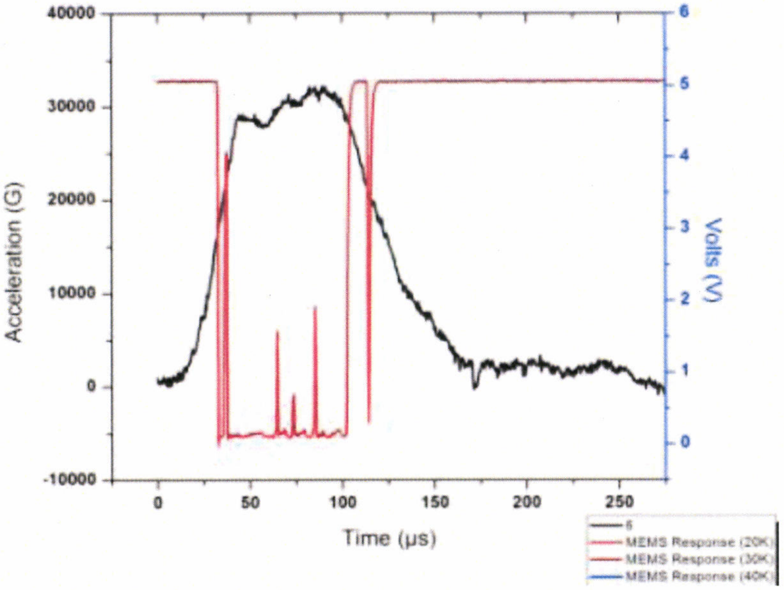

Figure 5: Parallel combination of five 20,000-g (640-µm long 70-µm wide) cantilevers triggering at 16,379 g

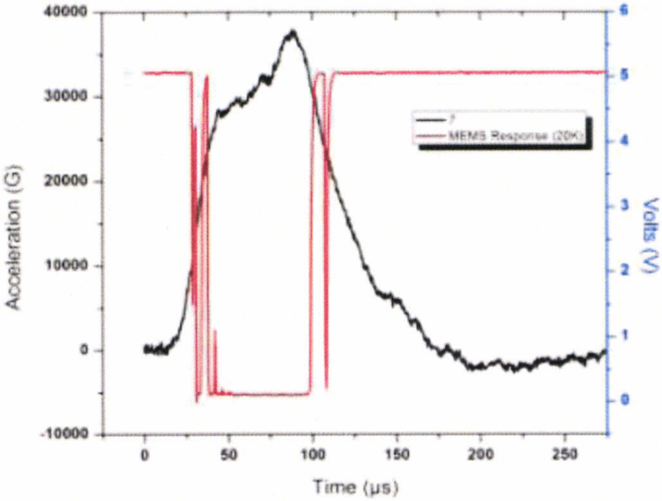

Figure 6: Parallel combination of five 20,000-g (640-µm long 70-µm wide) cantilevers triggering at 15,337 g

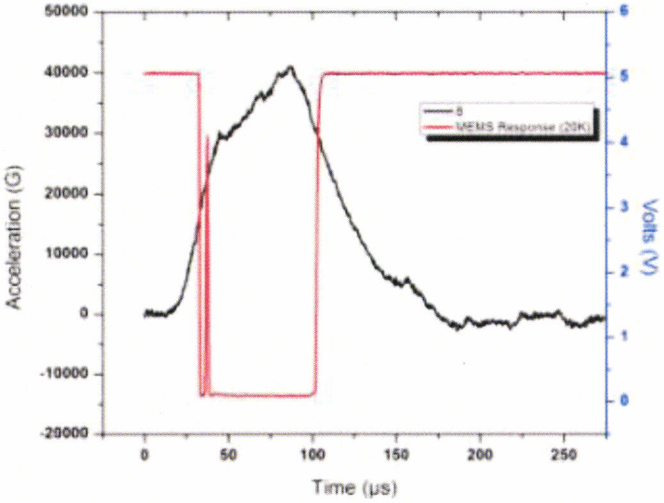

Figure 7: Parallel combination of five 20,000-g (640-µm long 70-µm wide) cantilevers triggering at 16,490 g

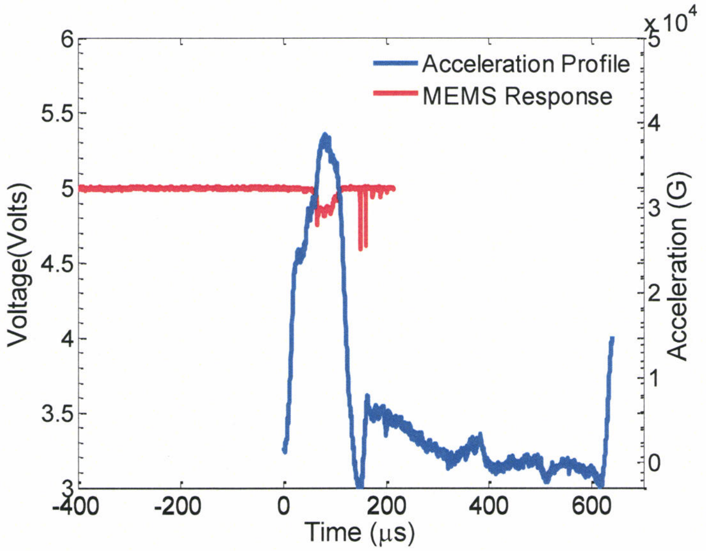

Figure 8: Parallel combination of five 30,000-g (572-µm long 70-µm wide) cantilevers triggering at 30,058 g for a peak applied profile of 38,570 g. High contact resistance due to contaminated contact

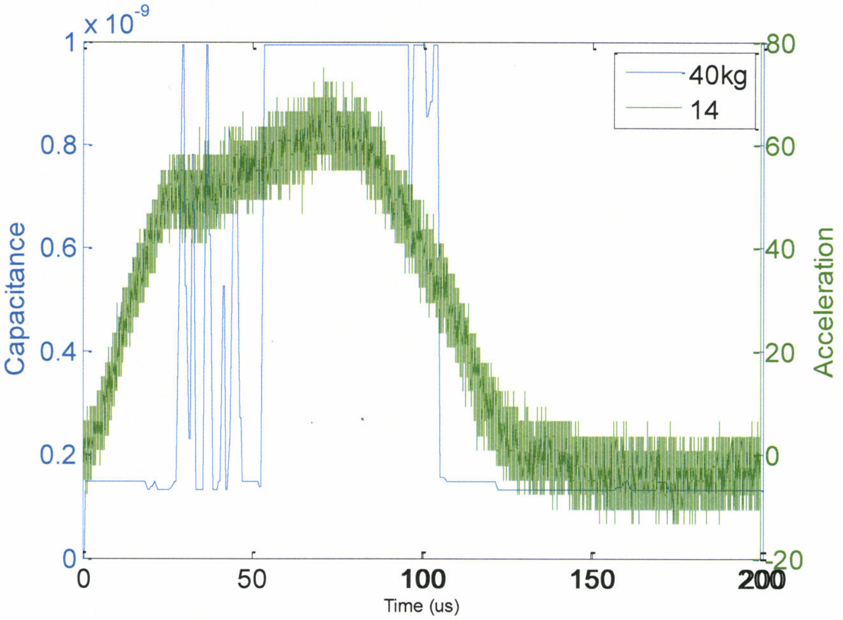

Figure 9: Capacitive response data of 40,000-g beams triggering at 43630 g for a applied acceleration profile of 63,000 g

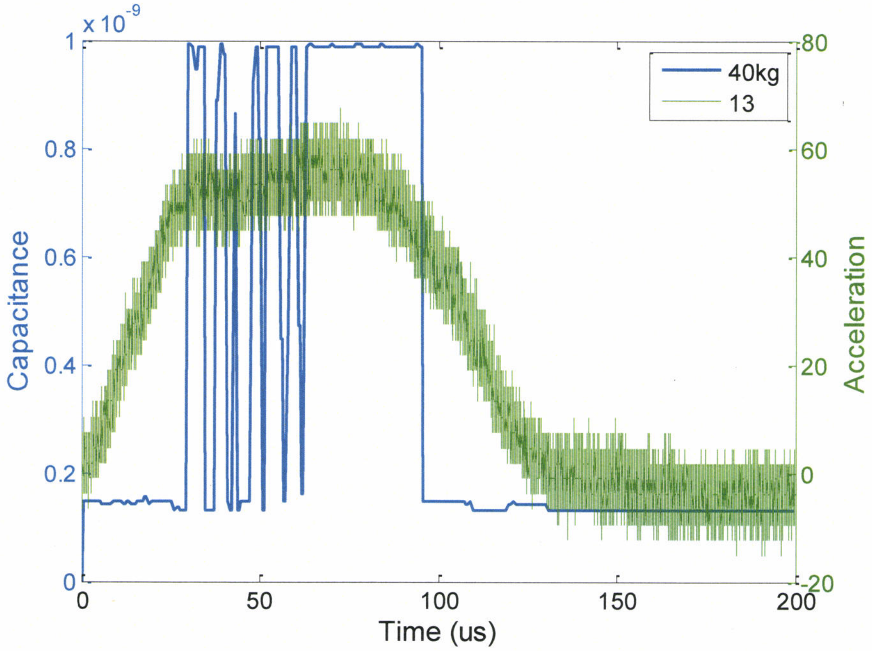

Figure 9: Capacitive response data of 40000-g beams triggering at 41910 g for an applied acceleration profile of 63,000 g

DEPARTMENT OF DEFENSE

DEFENSE TECHNICAL
INFORMATION CENTER
8725 JOHN J. KINGMAN ROAD,
SUITE 0944
FT. BELVOIR, VA 22060-6201
ATTN: DTIC/OCA

DEPARTMENT OF DEFENSE CONTRACTORS

EXELIS, INC.
1680 TEXAS STREET, SE
KIRTLAND AFB, NM 87117-5669
ATTN: DTRIAC